

Numerical quantification of the wind properties of cool main sequence stars

Judy J. Chebly ^{1,2*}, Julián D. Alvarado-Gómez ¹, Katja Poppenhäger ^{1,2}, Cecilia Garraffo ³,

¹Leibniz Institute for Astrophysics, An der Sternwarte 16, 14482, Potsdam, Germany

²Institute of Physics and Astronomy, University of Potsdam, Potsdam-Golm, 14476, Germany

³Harvard-Smithsonian Center for Astrophysics, 60 Garden Street, Cambridge, MA 02138, USA

Accepted XXX. Received YYY; in original form ZZZ

ABSTRACT

As a cool star evolves, it loses mass and angular momentum due to magnetized stellar winds which affect its rotational evolution. This change has consequences that range from the alteration of its activity to influences over the atmosphere of any orbiting planet. Despite their importance, observations constraining the properties of stellar winds in cool stars are extremely limited. Therefore, numerical simulations provide a valuable way to understand the structure and properties of these winds. In this work, we simulate the magnetized winds of 21 cool main-sequence stars (F-type to M-dwarfs), using a state-of-the-art 3D MHD code driven by observed large-scale magnetic field distributions. We perform a qualitative and quantitative characterization of our solutions, analyzing the dependencies between the driving conditions (e.g., spectral type, rotation, magnetic field strength) and the resulting stellar wind parameters (e.g., Alfvén surface size, mass loss rate, angular momentum loss rate, stellar wind speeds). We compare our models with the current observational knowledge on stellar winds in cool stars and explore the behaviour of the mass loss rate as a function of the Rossby number. Furthermore, our 3D models encompass the entire classical Habitable Zones (HZ) of all the stars in our sample. This allows us to provide the stellar wind dynamic pressure at both edges of the HZ and analyze the variations of this parameter across spectral type and orbital inclination. The results here presented could serve to inform future studies of stellar wind-magnetosphere interactions and stellar wind erosion of planetary atmospheres via ion escape processes.

Key words: exoplanets – stars: atmospheres – stars: magnetic fields – stars: mass-loss – stars: winds, outflows

1 INTRODUCTION

For many decades, scientists have known that the Sun has a mass outflow, which is most visible in the behavior of comet tails (e.g., Biermann 1957). It has also been established that solar wind is a natural byproduct of the heating processes that produce the hot solar corona ($T \sim 10^6$ K). As a result, all cool main-sequence stars ($M_{\star} \leq 1.3 M_{\odot}$) with analogous hot coronae, evidenced from their measured X-ray properties (Schmidt et al. 1995; Pizzolato et al. 2000; Wright et al. 2011a), should have similar winds (Parker 1958). Magnetic fields are thought to play a key role as an energy source for the corona and the expanding solar atmosphere (e.g., Aschwanden 2006; Klimchuk 2015; Velli et al. 2015). Recent theories have shown that in addition to magnetic fields, wave dissipation (via turbulence) and magnetic reconnection could also play a role in energizing and shaping the spatial properties of the solar wind (see, Ofman 2010; Cranmer 2012; Hansteen & Velli 2012; Cranmer et al. 2015).

Winds, even if relatively weak, play an important role in stellar evolution for stars of different spectral types causing the star to lose angular momentum and slow its rotation over time (Weber & Davis 1967; Skumanich 1972; Matt et al. 2012; Gallet & Bouvier 2013, 2015; Johnstone et al. 2015a,b; Ahuir et al. 2020). As a result,

the magnetic activities that constitute the space weather (i.e., stellar winds, flares, coronal mass ejections) will decrease with age in low-mass stars (Skumanich 1972; Güdel et al. 1997; Ribas et al. 2005; Vidotto et al. 2014a). These changes in the host star will also affect the evolution of planetary atmospheres and habitability (Tian 2008; Kislyakova et al. 2014; Airapetian et al. 2017).

Direct measurements of the solar wind by spacecraft such as the Advanced Composition Explorer (ACE, Stone et al. 1998; McComas et al. 1998), Ulysses (McComas et al. 2003), and Parker solar probe (Kasper et al. 2021) have improved our knowledge and understanding of its properties. On the other hand, detecting a solar-like wind emitted by another star has proven extremely challenging. This is not surprising, given how difficult it is to observe the solar wind remotely. The latter carries a very low mass loss rate ($\dot{M}_{\odot} = 2 \times 10^{-14} M_{\odot} \text{ yr}^{-1}$, see Feldman 1977; Wood 2004), which implies relatively low densities (near the heliopause: $\sim 0.002 \text{ cm}^{-3}$, Gurnett & Kurth 2019). Similarly, its high temperature and elevated ionization state, make it difficult to detect with simple imaging or spectroscopic techniques. As a result, properties such as the associated mass loss rates, angular momentum loss rates, and terminal velocities, crucial to understand stellar winds in low-mass stars, remain poorly constrained.

Attempts to directly detect thermal radio emission from the plasma stream in cool stars have not yet led to any discovery (Lim & White

* E-mail: jchebly@aip.de

1996; Drake et al. 1993; van den Oord & Doyle 1997; Gaidos et al. 2000; Villadsen et al. 2014; Fichtinger et al. 2017). Current radio telescopes are not optimized for this method; they can only detect winds much stronger than those from the Sun. Moreover, the coronae of these active stars are also radio sources, making it difficult to determine the exact source of the emission. Nevertheless, this method has been able to establish upper limits for solar analogs of $1.3 \times 10^{-10} \dot{M}_{\odot} \text{ yr}^{-1}$ (Gaidos et al. 2000; Fichtinger et al. 2017). Another proposed method for direct detection is to look for X-ray emission from nearby stars. As the star's winds propagate, they collide with the Local Interstellar Medium (ISM), forming "astrospheres" similar to the Sun's heliosphere (Wood 2004). The charge exchange between the highly ionized stellar wind and the ISM produces X-ray photons with energies ranging from 453 to 701 eV. However, this method was unable to detect circumstellar charge exchange X-ray emission even from the nearest star, Proxima Centauri (Wargelin & Drake 2002).

Similar to the charge exchange X-ray emission method, the Ly- α absorption technique assumes the presence of the charge exchange phenomenon. In this case, however, we are interested in the neutral hydrogen wall formed at the astrospherical outer boundary by the interaction between the stellar wind and the ISM. This exchange has been detected as excess HI Ly- α absorption in Hubble Space Telescope UV stellar spectra (Linsky & Wood 2014). With nearly 30 measurements to date, spectroscopic analyses of the stellar HI lines have proven to be the best method to unambiguously detect and measure weak solar-like winds as well as some evolved cool stars (Wood et al. 2021).

Using this method, Wood et al. (2005b) found evidence for some increase in \dot{M} with magnetic activity, corresponding to a power-law relation in the form $\dot{M} \propto F_X^{1.34 \pm 0.18}$ with $F_X < 10^6 \text{ erg cm}^{-2} \text{ s}^{-1}$. However, this relation does not seem to hold anymore for more active stars ($F_X > 10^6 \text{ erg cm}^{-2} \text{ s}^{-1}$), mainly M-dwarfs (Wood et al. 2005b, 2014). Recently, Wood et al. (2021) established a power law ($\dot{M} \propto F_X^{0.77 \pm 0.04}$) between the \dot{M} per unit surface area and the X-ray surface flux for coronal winds for a broader selection of stars, including G, K, and new \dot{M} estimates for M-dwarfs. They found that the relation breaks even for stars with $F_X < 10^6 \text{ erg cm}^{-2} \text{ s}^{-1}$ (e.g., GJ 436, which has $F_X = 4.9 \times 10^4 \text{ erg cm}^{-2} \text{ s}^{-1}$, where the \dot{M} was estimated by using the planet as a probe for the stellar wind Vidotto & Bourrier 2017) with the magnetic topology being a possible factor for the scatter.

While extremely useful, the search for astrospherical absorption is influenced by a number of critical factors. For instance, this method is strongly dependent on the relative velocity of the stellar rest frame and the ISM flow velocity (V_{ISM}). As well as on the angle, θ , between the upwind direction of the ISM flow and the line-of-sight to the star (Wood et al. 2021). It also requires prior knowledge of the properties of the ISM such as the density and its ionization state (Wood et al. 2005a; Redfield & Linsky 2008a). Finally, its applicability is limited to relatively nearby stars ($\lesssim 15 \text{ pc}$) due to the absorption of the ISM.

Due to the scarcity of observational data and associated limitations, numerical simulations can be used to improve our understanding of stellar winds. Models based on Alfvén waves are more commonly used to simulate the stellar wind from stars other than the Sun (Suzuki 2006). This is because these waves are considered to be key mechanism for heating and accelerating the solar wind (van der Holst et al. 2014; Van Doorselaere et al. 2020).

In this study, we present a detailed numerical characterization of the stellar wind properties of cool main-sequence stars (early F to M-dwarfs) covering a range of rotation rates and magnetic field strengths. We compute steady-state stellar wind solutions using a

state-of-the-art 3D MHD model and provide consistent qualitative and quantitative comparisons. Our goal is to better understand the different stellar wind properties as a function of the driving parameters, allowing us to explore the expected stellar wind conditions in the circumstellar region around planet-hosting stars.

This paper is organized as follows: Section 2 describes the numerical model and properties of the selected stellar sample. In Sect. 3, we present our numerical results, discuss the derived trends in the stellar wind properties, and compare our results with observations. This information is then used to quantify the stellar wind conditions and explore their implications in the context of the classical habitable zone (HZ) around cool main-sequence stars. Conclusions and summary are provided in Sect. 4.

2 MODEL DESCRIPTION

We simulate stellar winds in cool main-sequence stars using the state-of-the-art Space Weather Modeling Framework (SWMF; Sokolov et al. 2013; van der Holst et al. 2014; Gombosi et al. 2018). The SWMF is a set of physics-based models (from the solar corona to the outer edge of the heliosphere) that can be run independently or in conjunction with each other (Tóth et al. 2012). This model uses the numerical schemes of the Block Adaptive Tree Solar Roe-Type Upwind Scheme (BATS-R-US; Powell et al. 1999) MHD solver. For a detailed description of the model, see Gombosi et al. (2021). The multi-domain solution starts with a calculation using the Solar/Stellar Corona (SC) module which incorporates the Alfvén Wave Solar Model (AWSoM; van der Holst et al. 2014). This module provides a description of the coronal structure and the stellar wind acceleration region. The simulation is then coupled to a second module known as the Inner Heliosphere/Astrosphere¹ (IA). In this way, it is possible to propagate the stellar wind solution up to Earth's orbit and beyond. The model has been extensively validated and updated employing remote sensing as well as in-situ solar data (e.g., Oran et al. 2017; Sachdeva et al. 2019; van der Holst et al. 2019).

AWSoM is driven by photospheric magnetic field data, which is normally available for the Sun in the form of synoptic magnetograms (Riley et al. 2014). A potential field source surface method is used to calculate the initial magnetic field (more details in the following section). This information is used by AWSoM to account for heating and radiative cooling effects, as well as the Poynting flux entering the corona, and empirical turbulent dissipation length scales. With the interplay between the magnetic field distribution, the extrapolation of the potential field, and the thermodynamic properties, the model solves the non-ideal magnetohydrodynamic (MHD) equations for the mass conservation, magnetic field induction, energy (coronal heating), and momentum (acceleration of the stellar wind). These last two aspects are controlled by Alfvén waves propagating along and against the magnetic field lines (depending on the polarity of the field). In the momentum equation, the heat and acceleration contributions are coupled by an additional term for the total pressure and a source term in the energy equation. The numerical implementation is described in detail in van der Holst et al. (2014). Once these conditions are provided, the simulation evolves all equations locally until a global steady-state solution is reached.

¹ This module is formally labeled IH within the SWMF, but since we are working with low-mass main sequence stars, we will refer to it as the Inner Astrosphere (IA) domain.

Table 1. Fundamental parameters of our sample. Columns 1–8 list the star number, name, spectral type (SpT), stellar mass (M_{\star}), stellar radius (R_{\star}), rotation period (P_{rot}), effective temperature (T_{eff}), and luminosity, respectively (See et al. 2019a and references therein).

ID number	Star	SpT	M_{\star} [M_{\odot}]	R_{\star} [R_{\odot}]	P_{rot} [d]	T_{eff} [K]	L_{\star} [L_{\odot}]
1	τ Boo	F7V	1.34	1.46	3	6387	3.0
2	HD 179949	F8V	1.21	1.19	7.6	6168	1.80
3	HD 35296	F8V	1.06	1.1	3.48	6202	1.60
4	HN Peg	G0V	1.1	1.04	4.55	5974	1.20
5	HD 190771	G2V	1.06	1.01	8.8	5834 ± 50	0.99
6	TYC 1987-509-1	G7V	0.9	0.83	9.43	5550^{\dagger}	0.52 ± 0.03
7	HD 73256	G8V	1.05	0.89	14	5480^{\dagger}	0.72
8	HD 130322	K0V	0.79	0.83	26.1	5400^{\dagger}	0.5
9	HD 6569	K1V	0.85	0.76	7.13	5170	0.36 ± 0.01
10	ϵ Eri	K2V	0.85	0.72	11	5125 ± 87	0.3 ± 0.06
11	HD 189733	K2V	0.82	0.76	12.5	4939	0.34
12	HD 219134	K3V	0.81	0.78	42.2	4835^{\dagger}	0.27
13	TYC 6878-0195-1	K4V	0.65^{\ddagger}	0.64^{\ddagger}	5.72	4600^{\dagger}	0.8 ± 0.32
14	61 Cyg A	K5V	0.66	0.62	34.2	4655^{\dagger}	0.15
15	HIP 12545	K6V	0.58^{\ddagger}	0.57^{\ddagger}	4.83	4300^{\dagger}	0.4 ± 0.06
16	TYC 6349-0200-1	K7V	0.54^{\ddagger}	0.54^{\ddagger}	3.39	4100^{\dagger}	0.3 ± 0.02
17	DT Vir	M0V	0.59	0.53	2.85	3850^{\dagger}	0.055
18	GJ 205	M1.5V	0.63	0.55	33.6	3690^{\dagger}	0.061 ± 0.006
19	EV Lac	M3.5V	0.32	0.3	4.37	3267	0.013
20	YZ CMi	M4.5V	0.32	0.29	2.77	3129	0.012
21	GJ 1245 B	M6V	0.12	0.14	0.71	3030^{\S}	0.0016

‡ Reference from Vidotto et al. (2014b)

† Reference from Pecauc & Mamajek (2013)

§ Reference from Vidotto et al. (2013)

2.1 Simulation parameters and setup

In our work, we apply the SWMF/AWSoM model to main-sequence F, G, K, and M-type stars by assuming that their stellar winds are driven by the same process as the solar wind. We analyze the properties of the stellar wind by a coupled simulation covering the region of the stellar corona (SC, spherical) and the resulting structure within the inner astrosphere (IA, cartesian). Figure 1 illustrates the coupling procedure in one of our models. This coupling was necessary only in the case of F, G, and K stars, in order to completely cover the habitable zones (HZ)², which are larger and farther away from the star. Parameters such as stellar radius (R_{\star}), mass (M_{\star}), and rotation period (P_{rot}), are also taken into account in the simulations. We followed the approach in Kopparapu et al. (2014) in order to determine the optimistic HZs boundaries of each star in our sample.

2.1.1 Simulation domain

The star is positioned in the center of the SC spherical domain. The radial coordinate in SC ranges from $1.05 R_{\star}$ to $67 R_{\star}$, except for M-dwarfs, where it extends to $250 R_{\star}$. The choice of the outer edge value of the SC domain was chosen in a way to obtain both edges of the HZ in one domain. The habitable zones limits were calculated using Kopparapu et al. (2014) approach and the reported measured L_{\star} and T_{eff} for each star in our sample (see Table 1). As will be discussed in Sect. 3, in the case of M-dwarfs, the extension had to be performed in order to cover the entire Alfvén surface (AS)³, while keeping the default parameters for AWSoM fixed (see Sect. 2.1.3). The domain uses a radially stretched grid with the cartesian z-axis aligned with the rotation axis. The cell sizes in the meridional (ϕ) and azimuthal (θ) directions are fixed at $\sim 2.8^{\circ}$. The total number of cells in the SC domain is $\sim 8 \times 10^5$.

² The range of orbits around a star in which an Earth-like planet can sustain liquid water on its surface.

³ This structure sets the boundary between the escaping wind and the magnetically coupled outflows that do not carry angular momentum away from the star.

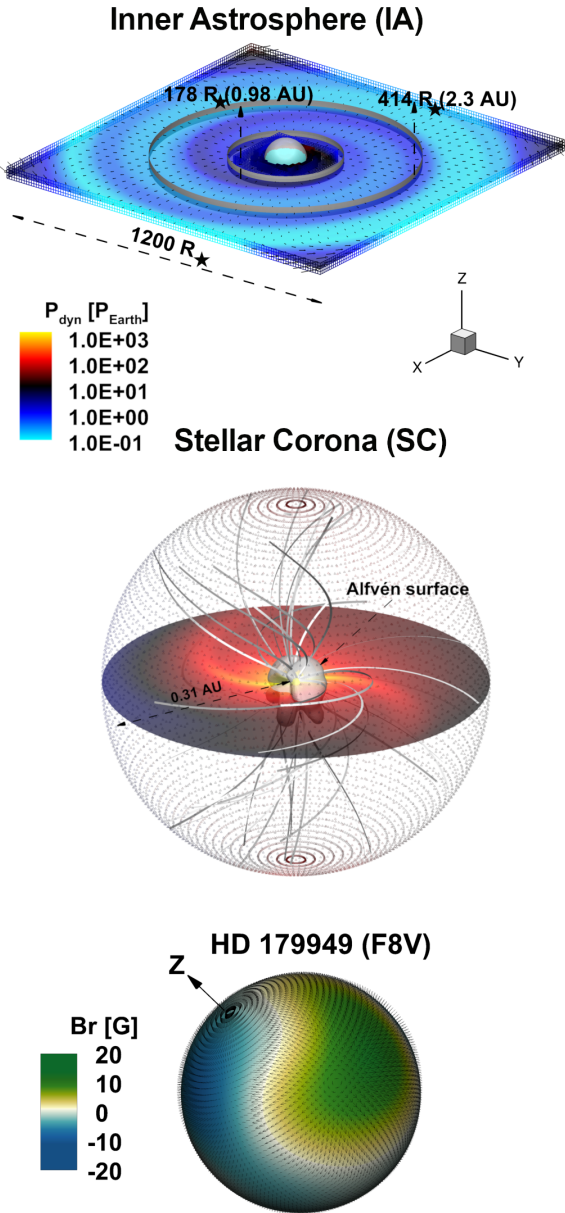


Figure 1. Simulated stellar wind environment for HD 179949 including multi-domain models. The bottom panel contains the surface field distribution (in Gauss) provided by the ZDI map and used to drive the AWSoM solution within the stellar corona (SC) domain (middle panel). The blue-green color bar represents the radial magnetic field strength on the stellar surface. Within SC, the gray iso-surface corresponds to the Alfvén surface of the stellar wind (see Sect. 3.1). Selected magnetic field lines are shown in white. The steady-state solution is propagated from the coupling region ($62 - 67R_{\star}$) to the entire Inner Astrosphere (IA) domain ($1200 R_{\star}$ in each cartesian direction; upper panel). The central gray sphere in the top panel denotes the boundary of IA with the SC domain at $67 R_{\star}$. This domain contains the inner and outer edges of the habitable zone (gray circles). Color-coded (top and middle panel) is the wind dynamic pressure ($P_{\text{dyn}} = \rho U^2$), normalized to the nominal Sun-Earth value (≈ 1.5 nPa), visualized on the equatorial plane of both domains. The z-axis indicates the assumed stellar rotation axis of the star.

The steady-state solutions obtained within the SC module are then used as inner boundary conditions for the IA component. An overlap of $5 R_{\star}$ (from $62 R_{\star}$ to $67 R_{\star}$) is used in the coupling procedure between the two domains for F, G, and K stars (more details on the necessity of the overlap when coupling between domains can be found in [Tóth et al. 2005](#)). The IA is a cube that extends from $62 R_{\star}$ to $600 R_{\star}$ in each cartesian component. Adaptive Mesh refinement (AMR) is performed within IA, with the smallest grid cell size of $\sim 1.17 R_{\star}$ increasing up to $9.37 R_{\star}$ with a total of 3.9 million cells. As the simulation evolves, the stellar wind solution is advected from SC into the larger IA domain where the local conditions are calculated in the ideal MHD regime.

2.1.2 Magnetic boundary conditions

In the initial condition of the simulation, observations are used to set the radial component of the magnetic field B_r [G] anchored at the base of the wind (at the inner boundary). As mentioned earlier, a finite potential field extrapolation procedure is carried out to obtain the initial configuration of the magnetic field throughout SC ([Tóth et al. 2011](#)). This procedure requires setting an outer boundary (source surface, r_s), beyond which the magnetic field can be considered to be purely radial and force-free. The magnetic field can therefore be described as a gradient of a scalar potential and determined by solving Laplace’s equation in the domain. For the simulations discussed here, we set r_s at 45% of the SC domain size for F, G, and K stars, and 70% for M-dwarfs. While the choice of this parameter does not alter significantly the converged solutions, it can modify the required run time of each model to achieve convergence. Therefore, our selection was done to guarantee convergence to the steady-state in a comparable number of iterations between all spectral types.

The stellar magnetic field as reconstructed from Zeeman Doppler Imaging (ZDI)⁴, is used as the inner boundary condition of SC (Fig. 2). Therefore, the resulting wind solutions are more realistic than models based on simplified/idealized field geometries ([Chebly et al. 2021](#)). Although the reconstructed maps provide the distribution of vector magnetic fields, we use only the radial component of the observed surface field. The magnetogram is then converted into a series of spherical harmonic coefficients with a resolution similar to that of the original map. The order of the spherical harmonics should be chosen so that artifacts such as the "ringing" effect do not appear in the solution ([Tóth et al. 2011](#)). In our models, we performed the spherical harmonics expansion up to $l_{\text{max}} = 5$.

2.1.3 Input parameters

After we set the initial conditions, we define several parameters for the inner boundary. In order to reduce the degree of freedom of the parameter set, we only modify the parameters related to the properties of the stars, such as mass, rotation period, and radius. As for the other parameters, we implement the same values that are commonly used in the solar case ([van der Holst et al. 2014](#); [Sachdeva et al. 2019](#)). The Poynting flux ($S/B_{\star} = 1.1 \times 10^6 \text{ J m}^{-2} \text{ s}^{-1} \text{ T}$) is a parameter that determines the amount of wave energy provided at the base of a coronal magnetic field line. The other parameter is the proportionality

⁴ A tomographic imaging technique that allows the reconstruction of the large-scale magnetic field (strength and polarity) at the star’s surface from a series of polarized spectra (see e.g., [Donati et al. 2006](#); [Morin et al. 2008](#); [Fares et al. 2009](#); [Alvarado-Gómez et al. 2015](#); [Hussain et al. 2016](#); [Kochukhov 2020](#)).

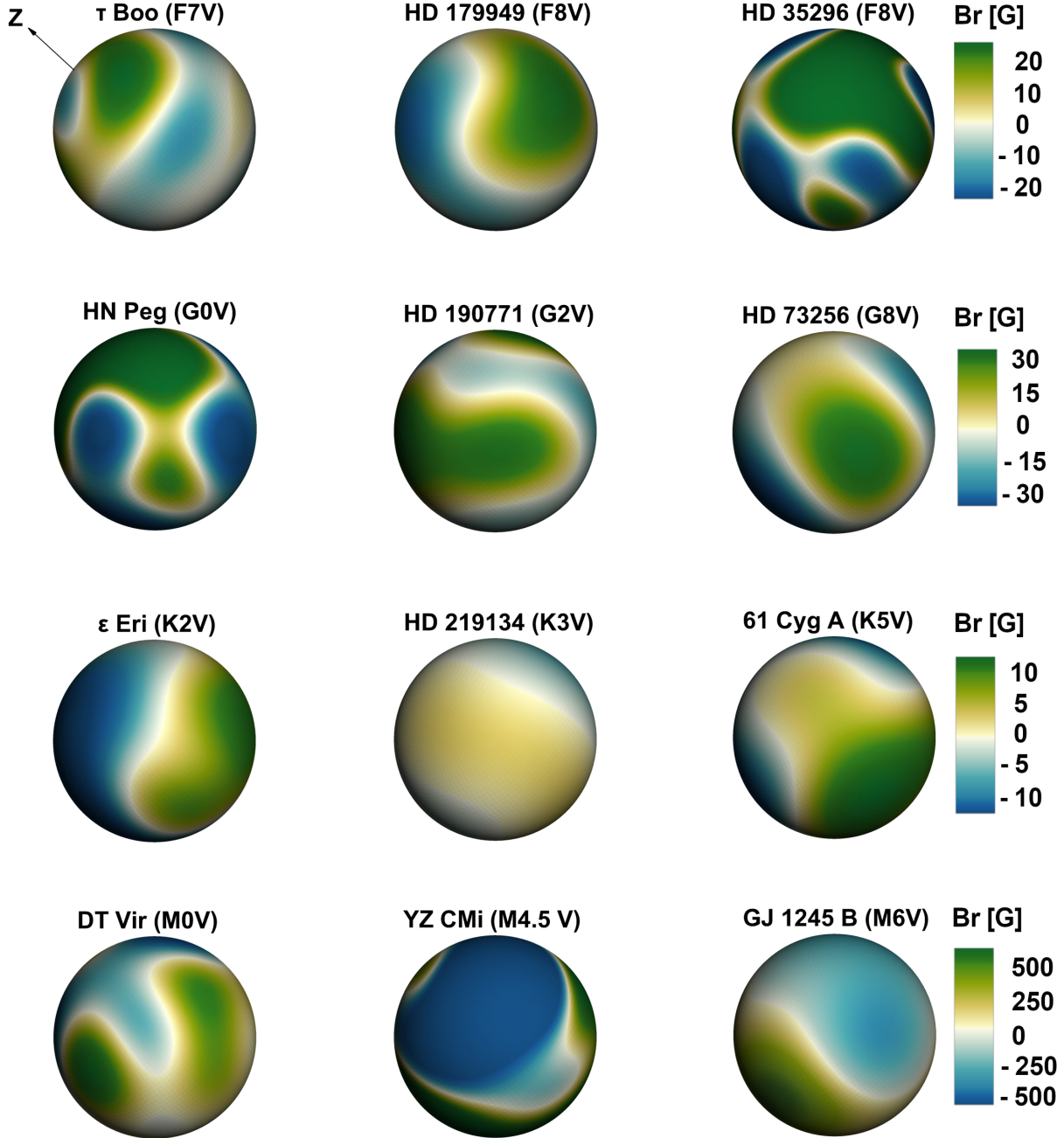


Figure 2. Examples of surface field distribution (in Gauss) of our sample stars retrieved from ZDI maps. The rows represent different spectral types going from late F-(top) to M-dwarfs (bottom) as indicated. The color-code represents the normalized radial magnetic field for a given row. The z-axis indicates the assumed stellar rotation axis for all the stars in the panel. The slowest rotation in our sample of 21 stars is HD 219134 (K3V, $P_{\text{rot}} = 42.2$ d), and the fastest is GJ 1245 B (M6V, $P_{\text{rot}} = 0.71$ d). The radial magnetic field strength ranges from 5 G to 1.5 kG.

constant that controls the dissipation of Alfvén wave energy into the coronal plasma and is also known as the correlation length of Alfvén waves ($L_{\perp} = 1.5 \times 10^5 \text{ m } \sqrt{T}$). We use the values given in Sokolov et al. (2013) to define the base temperature ($T_0 = 2 \times 10^6 \text{ K}$) and the base density ($n_0 = 2 \times 10^{11} \text{ cm}^{-3}$).

We note that the choice of these parameters will affect the simulation results, as reported in several studies that followed different approaches (e.g., Boro Saikia et al. 2020a; Jivani et al. 2023). Recently, Jivani et al. (2023) performed a global sensitivity analysis to quantify the contributions of model parameter uncertainty to the

variance of solar wind speed and density at 1 au. They found that the most important parameters were the photospheric magnetic field strength, S/B_{\star} , and L_{\perp} . Furthermore, in Boro Saikia et al. (2020a), an increase in the mass loss rate (\dot{M}_{\star}), and angular momentum loss rate (\dot{J}_{\star}) was reported when S/B_{\star} is increased from the solar value to $2.0 \times 10^6 \text{ J m}^{-2} \text{ s}^{-1} \text{ T}$, which is expected because S/B_{\star} drives the energy of the Alfvén wave, resulting in higher \dot{M}_{\star} and \dot{J}_{\star} .

In this work, however, we are interested in isolating the expected dependencies with the relevant stellar properties (e.g., mass, radius, rotation period, photospheric magnetic field) which can only be an-

alyzed consistently if the AWSoM related parameters are kept fixed between spectral types. Moreover, as will be discussed in detail in Sect. 3.3, the results obtained using the standard AWSoM settings are either consistent with current stellar wind observational constraints for different types of stars or the apparent differences can be understood in terms of other physical factors or assumptions made in the observations. For these reasons, we have chosen not to alter these parameters in this study, which also reduces the degrees of freedom in our models.

2.2 The sample of stars

Our investigation is focused on main sequence stars, with effective temperatures ranging from 6500 K down to 3030 K, and masses $M_{\star} < 1.34 M_{\odot}$ (spectral types F to M). All of these stars are either fully or partially convective. We use a sample of 21 stars whose large-scale photospheric magnetic fields were reconstructed with ZDI (See et al. 2019b and references therein). Some of these stars were observed at different epochs. In this case, the ZDI map with the best phase coverage, signal-to-noise ratio, and most spectra used in the reconstruction was chosen. The sample includes radial magnetic field strengths in the ZDI reconstruction between 5 G and 1.5 kG corresponding to HD 130322 (K0V) and EV Lac (M3.5V), respectively. Spectral types range from F7 (τ Boo, $M_{\star} = 1.34 M_{\odot}$, $R_{\star} = 1.46 R_{\odot}$) to M6 (GJ 1245 B, $M_{\star} = 0.12 M_{\odot}$, $R_{\star} = 0.14 R_{\odot}$). The rotation periods vary between fractions of a day to tens of days, with GJ 1245 B (M6V) having the shortest rotation period ($P_{\text{rot}} = 0.71$ d) and HD 219134 (K3V) the longest one ($P_{\text{rot}} = 42.2$ d). Table 1 contains the complete list of the sample stars and a summary of the stellar properties incorporated in our models.

3 RESULTS & DISCUSSION

3.1 The effect of star properties on the wind structure

The Alfvén surface (AS) is defined by the collection of points in the 3D space that fulfils the Alfvén radius criterion⁵. Numerically, it is determined by finding the surface for which the wind velocity reaches the local Alfvén velocity, $v_A = B/\sqrt{4\pi\rho}$, where B and ρ are the local magnetic field and plasma density, respectively. The Alfvén surface can be interpreted as the lever arm of the wind torque –the "position" at which the torque acts to change the angular rotation of the star⁶. The Alfvén Surface is used in numerical models to characterize (\dot{M}_{\star}) and (\dot{J}_{\star}) (e.g., Vidotto et al. 2015; Boro Saikia et al. 2020a; Garraffo et al. 2015b; Alvarado-Gómez et al. 2016). We compute \dot{J}_{\star} by performing a scalar flow rate integration over the AS and another one over a closed spherical surface (S) beyond the AS to determine \dot{M}_{\star} :

$$\dot{M}_{\star} = \int_S \rho(\mathbf{u} \cdot d\mathbf{A}) \quad (1)$$

$$\dot{J}_{\star} = \int_{AS} \Omega \rho R^2 \sin^2 \theta (\mathbf{u} \cdot d\mathbf{A}) \quad (2)$$

⁵ The Alfvén radius (R_A) is defined as the distance around a star at which the kinetic energy density of the stellar wind equals the energy density of the astrospheric magnetic field.

⁶ In other words, the angular momentum per unit mass within the stellar wind can be computed as if there were solid body rotation, at an angular velocity $\Omega_{\star} = 2\pi/P_{\text{rot}}$, out as far as the Alfvén surface.

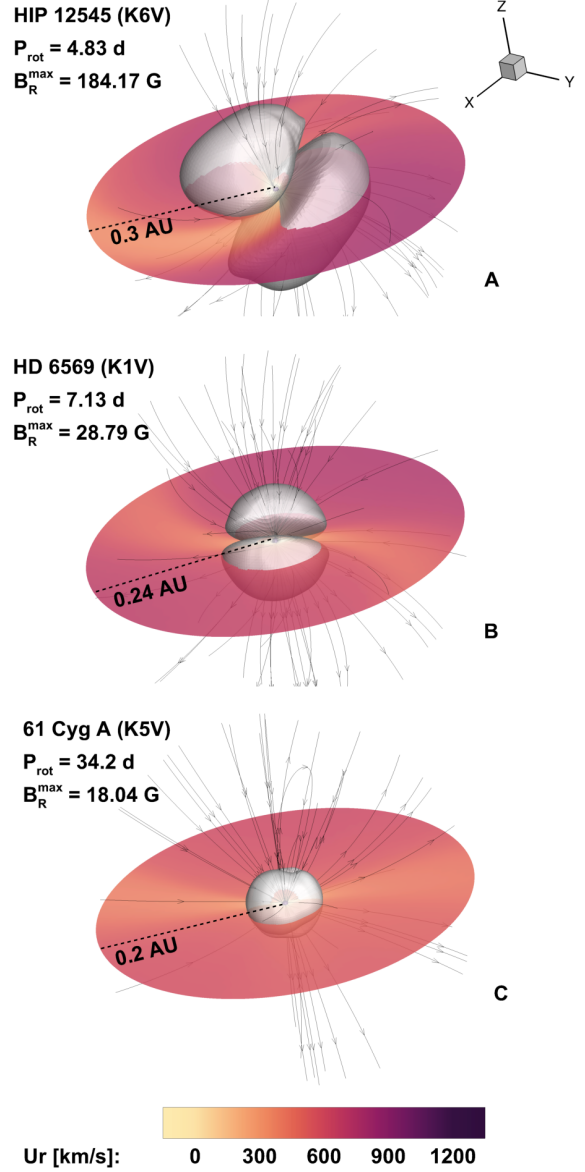


Figure 3. Simulation results in the SC domain for 3 K stars: HD 12545 (panel A), HD 6569 (panel B), 61 Cyg A (panel C) driven by ZDI magnetic field maps. All panels contain the projection onto the equatorial plane ($z = 0$) of the radial wind velocity (U_r). The translucent gray shade denotes the Alfvén surface calculated from the steady-state solution. The corresponding color scale U_r is preserved among the different panels. Selected 3D magnetic field lines are shown in black. The absolute size of the SC domain is indicated in each case.

Here \dot{J}_{\star} is the component of the change in angular momentum in the direction of the axis of rotation. The distance to the Alfvén surface is represented by R . The angle between the lever arm and the rotation axis is denoted by θ , which depends on the shape/orientation of the AS with respect to the rotation axis (and accounted for in the surface integral). The stellar angular velocity is represented by $\Omega = 2\pi/P_{\text{rot}}$. The surface element is denoted by $d\mathbf{A}$.

Figure 3 shows the AS of the stellar wind, with plasma streamers along with the equatorial section flooded with the wind velocity (U_r) for three K stars in our sample (HIP 12545, HD 6569, 61 Cyg A). If we compare two stars with similar P_{rot} but different B_R^{max} , we can

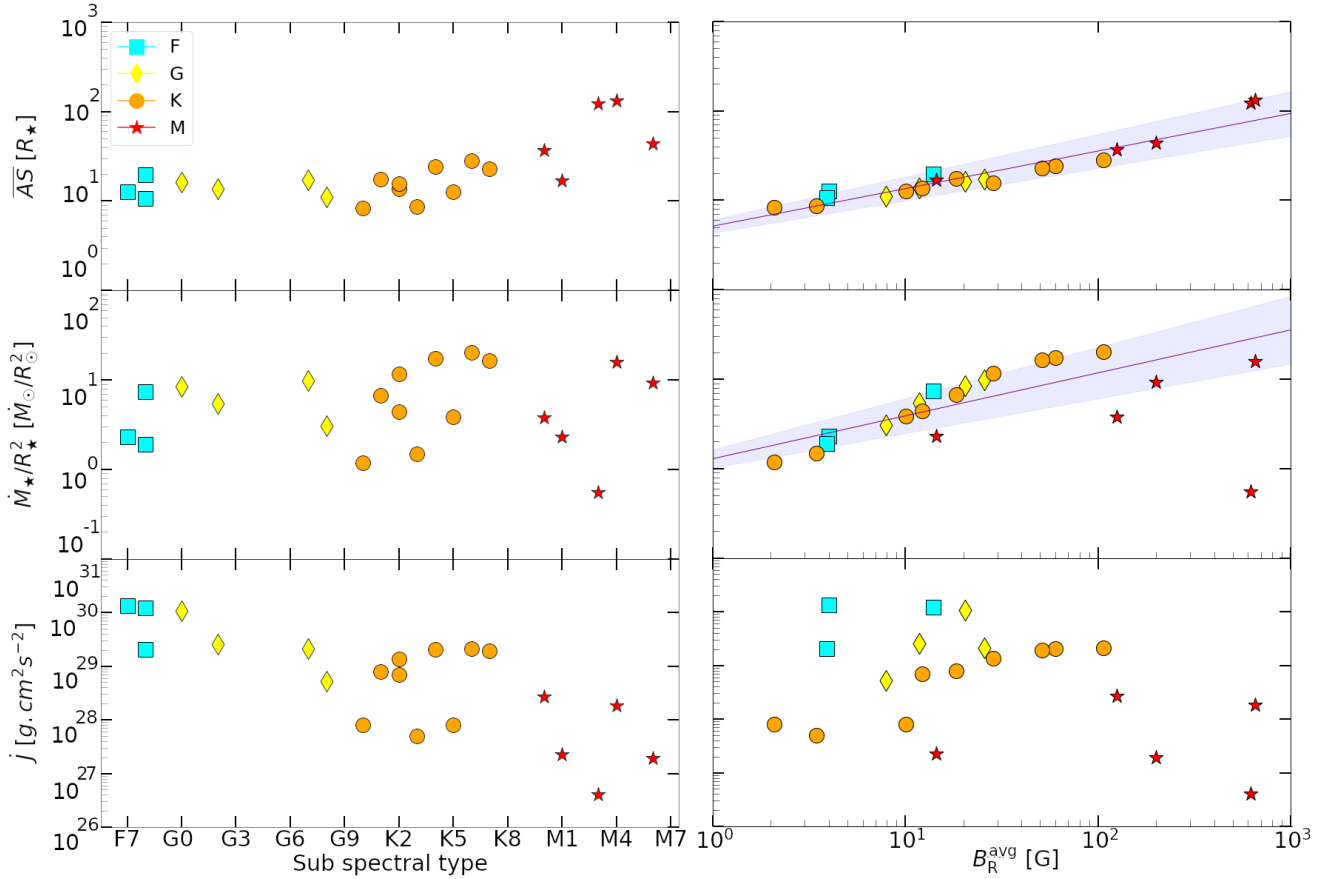


Figure 4. Simulated average Alfvén surface (\overline{AS} , top), mass loss rate per unit surface area (\dot{M}_\star/R_\star^2 , middle), and angular momentum loss rate (\dot{J} , bottom) as a function of the spectral type (left) and the surface-average radial magnetic field (B_R^{avg} , right). The mass loss rate is expressed in units of the average solar values ($\dot{M}_\odot = 2 \times 10^{-14} M_\odot \text{ yr}^{-1} = 1.265 \times 10^{12} \text{ g s}^{-1}$), normalized to the surface area of each star ($A_\star = 4\pi R_\star^2$). Individual points denote the results of each simulation presented in Sect. 3, Table 2. The different symbols and colors represent the spectral types (F, cyan/squares; G, yellow/diamonds; K, orange/circles; M, red/star). The purple line and shaded area represent the fitted power-law with its uncertainties.

clearly see that the size of AS increases with increasing magnetic field strength. This is a direct consequence of the dependence of the Alfvén velocity on these quantities (Eq. 1) and the distance from the star at which the Alfvén velocity is exceeded by the wind. For instance, for very active stars with stronger magnetic fields, the expected coronal Alfvén velocity is greater than for less active stars, increasing the radial distance that the wind velocity must travel to reach the Alfvén velocity. The associated Alfvén surface has a characteristic two-lobe configuration (Fig. 3, gray translucent area), with average sizes of $27 R_\star$, $18 R_\star$ and $13 R_\star$ for HIP 12545, HD 6569, and 61 Cyg A, respectively (see Table 2).

When we compare two stars with similar magnetic field strengths but different P_{rot} (see Fig. 3, panels B and C), the change in AS size is not as dramatic. The rotation period has primarily a geometric effect on the resulting AS. The Alfvén surface assumes a different tilt angle in all three cases. This tilt is mainly connected to the open magnetic field flux distribution on the star’s surface (Garraffo et al. 2015a). We also notice in Fig. 3 that the stellar wind distribution is mainly bipolar with a relatively fast component reaching up to $\sim 891 \text{ km s}^{-1}$ for HIP 12545 $\sim 702 \text{ km s}^{-1}$ for HD 6569, and $\sim 593 \text{ km s}^{-1}$ for 61 Cyg A. In section 3.3.1 we will discuss further the relation between the wind velocity with regard to P_{rot} and B_R .

Figure 4 shows the \dot{M}_\star , \dot{J} , \overline{AS} as estimated by the previously de-

scribed method, against the sub-spectral type of our star sample (left column) and the average radial magnetic field strength (B_R^{avg} , right column). Similar relations have been obtained for the maximum radial magnetic field strength and are presented in Appendix A. The average Alfvén surface size was calculated by performing a mean integral over the radius at each point of the 3D AS. The extracted quantities are represented by different colors and symbols for each spectral type (F, G, K, and M).

As expected, the AS increases as we move toward more magnetically active stars (Fig. 4, top-right panel). From our simulations, we were able to establish a relation between AS and B_R^{avg} using the bootstrap technique (1000 realizations) to find the mean of the slope and the intercept along with their uncertainties. We use this approach to determine all relations from our simulations. The relation is as follows:

$$\log \overline{AS}_R = (0.42 \pm 0.06) \log B_R^{\text{avg}} + (0.71 \pm 0.07) \quad (3)$$

Our simulated steady-state \dot{M}_\star show a scatter within the range [$0.5 \dot{M}_\odot/R_\odot^2$, $30 \dot{M}_\odot/R_\odot^2$], which is comparable to that estimated from the observed Ly α absorption method of G, K, and M-dwarfs in Wood et al. (2021). The variations in \dot{M}_\star are related to differences in the strength and topology of the magnetic field driving the

simulations (see Alvarado-Gómez et al. 2016; Vidotto et al. 2016; Evensberger et al. 2022), as well as to the Alfvén wave energy transfer to the corona and wind implemented in the model (Boro Saikia et al. 2020b; Jivani et al. 2023). For this reason, we tried to isolate the effects introduced by the star (e.g., M_\star , R_\star , P_{rot} , magnetic field strength) over the ones from the Alfvén wave heating (i.e., n_o , T_o , S/B_\star , L_\perp).

In terms of mass loss rate, stronger winds are expected to be generated by stronger magnetic fields (see Fig. 4) implying that the winds are either faster or denser. This interplay determines \dot{M}_\star (Eq. 1), which increases with increasing magnetic field strength regardless of spectral type. We see a common increase for F, G, K, and M-dwarfs (excluding EV Lac) in the saturated and unsaturated regime that can be defined from the simulations as follows:

$$\log \dot{M}_\star / R_\star^2 = (0.48 \pm 0.09) \log B_R^{\text{avg}} + (0.11 \pm 0.10) \quad (4)$$

On the other hand, we observe a slightly different behavior for M-dwarfs, whose \dot{M}_\star and \dot{J}_\star values tend to be lower. As discussed by Garraffo et al. (2018), the magnetic field complexity could also affect \dot{M}_\star for a given field strength. We consider this possibility in the following section. Note that, as has been shown in previous stellar wind studies of M-dwarfs (e.g., Garraffo et al. 2017; Kavanagh et al. 2021; Alvarado-Gómez et al. 2022b), modifications to the base AWSOM parameters (either in terms of the Poynting flux or the Alfvén wave correlation length) would lead to strong variations in \dot{M}_\star . This would permit placing the M-dwarfs along the general trend of the other spectral types in particular, the \dot{M}_\star value obtained for the star with the strongest B_R in our sample (EV Lac). While these modifications have physical motivations behind them (i.e. increased chromospheric activity, stronger surface magnetic fields), in most regards, they remain unconstrained observationally. Furthermore, the values we obtain in our fiducial AWSOM models are still within the range of observational estimates available for this spectral type (see Sect. 3.3.1), with the added benefit of minimizing the degrees of freedom and isolating the effects of the stellar parameters on the results.

Similarly, we see a large scatter of \dot{J}_\star with respect to the spectral type (Fig. 4, bottom left column), ranging from $10^{26} \text{ g cm}^2 \text{ s}^{-2}$ to $10^{31} \text{ g cm}^2 \text{ s}^{-2}$. This range is within the expected \dot{J}_\star values estimated for cool stars with the lowest value corresponding to M-dwarfs (See et al. 2019c and references therein). The maximum \dot{J}_\star values reached in our simulations are comparable to \dot{J}_\odot reached at solar minimum and maximum (7×10^{30} and $10 \times 10^{30} \text{ g.cm}^2\text{s}^{-2}$, Finley et al. 2018; Boro Saikia et al. 2020a). We note that this is the only parameter for which we have retained units in absolute values (as is commonly done in solar/stellar wind studies; see Cohen et al. 2010; Garraffo et al. 2015a; Finley et al. 2018). Using absolute units, we expect a decrease in \dot{J}_\star as we move from F to M-dwarfs, since \dot{J}_\star is a function of R^2 (Eq. 2). The scatter around this trend is dominated by the relatively small \dot{M}_\star values, the distribution of Ω_\star in our sample (variations up to a factor of 5), and the equatorial AS size where the maximum torque is applied ($\sin \theta$ in Eq. 2).

We also note that the sample is biased toward weaker magnetic field strengths. To better estimate how the magnetic field affects the properties of the stellar winds, we need a larger sample, not only in terms of stellar properties but also with stellar wind constraints such as \dot{M}_\star . The latter is so far the only stellar wind observable parameter for which comparisons can be made. For this reason, we will focus on the behavior of the \dot{M}_\star as a function of different stellar properties in the following sections of the analysis.

3.2 Stellar mass-loss rate and complexity

Coronal X-ray luminosity is a good indicator of the level of magnetic activity of a star and the amount of material heated to 10^6 K temperatures. The dependence of magnetic activity on dynamo action (i.e., dynamo number $D = R_o^{-2}$, Charbonneau 2020) has led a number of authors to use the Rossby number to characterize stellar activity, for a wide range of stellar types (Wright et al. 2011a). The Rossby number is defined as $R_o = P_{\text{rot}}/\tau_c$, where P_{rot} is the stellar rotation period and τ_c is the convective turnover time (Noyes et al. 1984; Jordan & Montesinos 1991; Wright et al. 2011b). We adopted the approach of Wright et al. (2018a) to calculate τ_c . In this case, the latter is only a function of the stellar mass (M_\star):

$$\log \tau_c = 2.33 - 1.50(M_\star/M_\odot) + 0.31(M_\star/M_\odot)^2 \quad (5)$$

As it was mentioned in Sect. 1, the study of Wood et al. (2021) suggests that coronal activity increases with M_\star . The overall increase in \dot{M}_\star with X-ray flux F_X ($\dot{M}_\star \propto F_X^{0.77 \pm 0.04}$), is most likely due to their dependence on magnetic field strength (see Sect. 3.1). However, they report a scatter of about two orders of magnitude of \dot{M}_\star around the trend line. This suggests that coronal activity and spectral type alone do not determine wind properties. The geometry of the magnetic field may also play a role.

The correlation between \dot{M}_\star and magnetic complexity has already been suggested by Garraffo et al. (2015b), which could in principle contribute to the scatter in (Wood et al. 2021, Fig. 10). The large-scale distribution of the magnetic field on the stellar surface is mainly determined by the rotation period and the mass of the star, namely R_o (Garraffo et al. 2018; Morin et al. 2010; Gastine et al. 2013). The Rossby number was used to determine the complexity function in Garraffo et al. (2018), which was able to reproduce the bimodal rotational morphology observed in young open clusters (OCs). The complexity function of Garraffo et al. (2018) is defined as

$$n = \frac{a}{R_o} + 1 + bR_o. \quad (6)$$

The constant 1 reflects a pure dipole. The coefficients $a = 0.02$ and $b = 2$ are determined from observations of OCs. The first term is derived from the ZDI map observation of stars with different spectral types and rotation periods. The third term is motivated by Kepler's observations of old stars (van Saders et al. 2016, 2019, 2016, 2019).

We emphasize that the complexity number (n), estimated from Eq. 6, differs from the complexity derived from the ZDI maps themselves (e.g., Garraffo et al. 2022). The complexity number from R_o is expected to be higher. This is due to the fact that many of the small-scale details of the magnetic field are not captured by ZDI.

We expect to lose even more information about the complexity of the field given that the ZDI maps are not really available to the community (apart from the published images). Image-to-data transformation techniques (which we applied to extract the relevant magnetic field information from the published maps) can lead to some losses of information, both spatially and in magnetic field resolution. These vary depending on the grid and the projection used to present the ZDI reconstructions (i.e., Mercator, flattened-polar, Mollweide). Using the star's raw ZDI map would prevent these issues and would aid with the reproducibility of the simulation results.

Finally, note that the expected complexity is also independent of the spherical harmonic expansion order used to parse the ZDI information to the simulations. The obtained R_o and n values for each star in our sample are listed in Table 2.

Figure 5 shows the behaviour of coronal activity and \dot{M}_\star with respect to the expected magnetic field complexity (n). The coronal

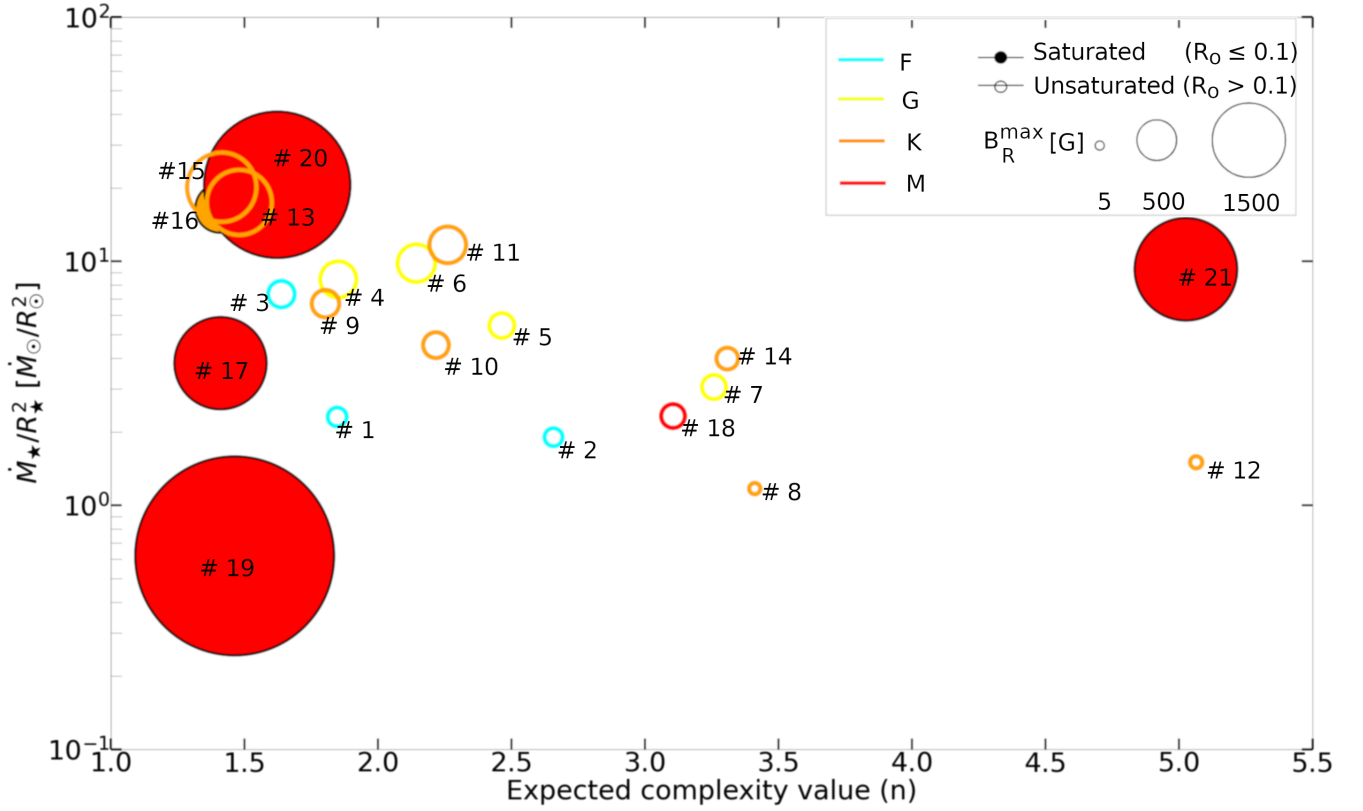


Figure 5. Simulated mass loss rate (\dot{M}_\star/R_\star^2) versus the expected complexity value (n , Garraffo et al. 2018) given the Rossby number (R_o) of each star. The mass loss rate is expressed in solar units, normalized by the unit surface area of each star. Individual points denote the results of each simulation presented in Sect. 3 (Table 2). The different colors (cyan, orange, yellow, red) represent the different spectral types respectively (F, G, K, and M). The filled circles and the empty ones represent stars in the saturated and unsaturated regimes, respectively. The symbol size denotes the maximum magnetic field strength (B_R^{\max}) in each case. The numbers refer to the ID of the star in our sample. The complexity value $n = 1$ corresponds to the dipole, and n increases as we move to the right.

activity is denoted by full and empty symbols corresponding to saturated and unsaturated stars, respectively. We consider stars with $R_o \leq 0.1$ in the saturated regime and stars with $R_o > 0.1$ in the unsaturated regime based on X-ray observations (Pizzolato et al. 2003; Wright et al. 2011b; Wright et al. 2018b; Stelzer et al. 2016; Wright & Drake 2016). The colors correspond to the different spectral types, whereas the numbers indicate the ID of each star in our sample. The symbol size represents the maximum radial magnetic field strength of each star extracted from the ZDI observations.

We anticipate seeing a trend in which the \dot{M}_\star decreases as the magnetic field complexity increases (leading to an increment of closed loops on the stellar corona), for stars in saturated and unsaturated regimes. For instance, ϵ Eri (#10, $B_R^{\max} = 25$ G, $n = 2.21724$) has an $\dot{M}_\star = 4.53 \dot{M}_\odot/R_\odot^2$ lower than HD 6569 (#9, $B_R^{\max} = 29$ G, $n = 1.80346$) with $\dot{M}_\star = 6.70 \dot{M}_\odot/R_\odot^2$. This is also true for τ Boo and HD 179949 where τ Boo (#1, $B_R^{\max} = 14$ G, $n = 1.84728$, $\dot{M}_\star = 2.30 \dot{M}_\odot/R_\odot^2$) has a higher \dot{M}_\star compared to HD 179949 (#2, $B_R^{\max} = 12$ G, $n = 2.65746$, $\dot{M}_\star = 1.90 \dot{M}_\odot/R_\odot^2$).

We also noticed that as we go to more active stars, like in the case of M-dwarfs, the field strength starts to dominate over the complexity in terms of contribution to the \dot{M}_\star . For example, GJ 1245 B (#21, $B_R^{\max} = 404$ G, $n = 5.02602$, $\dot{M}_\star = 9.27 \dot{M}_\odot/R_\odot^2$) has an \dot{M}_\star higher than DT Vir even though the complexity of the former is almost 5 times higher (DT Vir, #17, $B_R^{\max} = 327$ G, $n = 1.41024$,

$\dot{M}_\star = 3.81 \dot{M}_\odot/R_\odot^2$). However, in order to better understand the contribution of the complexity in \dot{M}_\star , we will need to run simulations for a wider range of stars with sufficiently high resolution of the driving magnetic field to capture directly the complexity of the field (and not estimate it from a scaling relation as it was performed here).

Moreover, our results show that whenever we have a case in which the star properties (M_\star , R_\star , and P_{rot}), magnetic field strength and complexity are comparable, we end up with similar \dot{M}_\star . This will be the case of TYC 6878-0195-1 (#13, $B_R^{\max} = 162$ G, $n = 1.48069$, $\dot{M}_\star = 17.42 \dot{M}_\odot/R_\odot^2$) and HIP 12545 (#15, $B_R^{\max} = 184$ G, $n = 1.41505$, $\dot{M}_\star = 20.11 \dot{M}_\odot/R_\odot^2$).

Furthermore, two stars with similar coronal activity with respect to X-ray flux, i.e., EV Lac and YZ CMi ($F_X \approx 10^7$ ergs $\text{cm}^{-2}\text{s}^{-1}$), but with slightly different magnetic field complexity, result in different wind properties: respectively $\dot{M}_\star = 0.62 \dot{M}_\odot/R_\odot^2$, and $\dot{M}_\star = 20.57 \dot{M}_\odot/R_\odot^2$. A similar situation occurs when two stars have a comparable field complexity but different coronal activity i.e., YZ CMi and GJ 205 (#18, $\dot{M}_\star = 2.32 \dot{M}_\odot/R_\odot^2$, $F_X \approx 10^5$ ergs $\text{cm}^{-2}\text{s}^{-1}$).

The lowest \dot{M}_\star corresponds to the saturated M-dwarf EV Lac (#19), which has the strongest B_R (1517 G) and one of the simplest complexities in our sample ($n = 1.46331$). The low complexity of the field means that the wind is dominated by open field lines, leading to very high wind velocities in the standard AWSoM model, but with a very low density, which in turn leads to small \dot{M}_\star

values. We remind the reader that the base density of the stellar wind is fixed at the stellar surface and is the same for all the stars in the sample (Sect. 2.1.3).

3.3 Stellar wind mass-loss rate and Rossby number

Using the results of our stellar winds models, we can study how the \dot{M}_\star changes as a function of the Rossby number (R_o). The Rossby number is a useful quantity because it not only removes the dependence on spectral type, but also relates the rotation period to magnetic field strength, complexity, and even stellar coronal activity. The latter is also important because cool stars exhibit a well-defined behavior between L_X (or F_X) and R_o (saturated and unsaturated regimes). Thus, if we analyze \dot{M}_\star using this parameter, we can see (to some extent) all dependencies simultaneously.

Figure 6 shows the stellar mass-loss rate per unit surface area (\dot{M}_\star/R_\star^2) as a function of the Rossby number (R_o). The circles show our 3D MHD numerical results, while the empty, filled, and the plus sign within a square corresponds to observational estimates of astrospheres (Wood et al. 2021), slingshot prominences (Jardine & Collier Cameron 2019), and absorption during an exoplanetary transit (Vidotto & Bourrier 2017), respectively. We use the same method as for the simulated stars (Eq. 5) to calculate the R_o of stars with constraints on their mass loss rate. Spectral types are indicated by different colors: cyan (F), yellow (G), orange (K), and red (M). The Sun is represented by a yellow star symbol. Dashed lines connect the common stars in our models and the observations. In this section, we will focus only on the resulting \dot{M}_\star from the numerical results.

As was mentioned earlier, our 3D MHD simulated \dot{M}_\star values are in the same range as the \dot{M}_\star estimates from the Ly- α astrospheric absorption method. Note that since we are only simulating steady-state stellar winds, our comparison is mostly focused on the steady mass loss \dot{M}_\star (filled squares and squares with a plus sign). As such, it is not surprising that our \dot{M}_\star values appear 1 - 2 orders of magnitude below the estimates associated with sporadic mass loss events such as slingshot prominences in very active stars in the saturated regime (filled squares, Jardine & Collier Cameron 2019).

Based on the relation between F_X and R_o (Wright et al. 2018a), and the broad correlation observed between \dot{M}_\star and F_X (Wood et al. 2021), we expect to see traces of a two-part trend (albeit with significant scatter) between \dot{M}_\star and R_o : a flat or saturated part that is independent of stellar rotation ($R_o \lesssim 0.1$, rapidly rotating stars), and a power law showing that the stellar wind mass loss rate decreases with increasing R_o ($R_o > 0.1$, slowly rotating stars).

For stars in the unsaturated regime, we do see a trend in which \dot{M}_\star increases with decreasing R_o . The relationship between \dot{M}_\star and R_o retrieved from our simulations is

$$\log \dot{M}_\star/R_\star^2 = (-1.13 \pm 0.23) \log R_o + (0.50 \pm 0.07). \quad (7)$$

The majority of the \dot{M}_\star derived from observation appears to follow the established relationship \dot{M}_\star - R_o , with some scatter within the error range. We do, however, notice four outliers, including three K stars and one G star. The K stars with the high \dot{M}_\star correspond to the binary 70 Oph A (K0V) and 70 Oph B (K5V). As for the 3rd K star and the G star, they correspond to evolved stars: δ Eri (K0IV, $\dot{M}_\star = 0.6 \dot{M}_\odot/R_\odot^2$, $R_o \sim 21$) and DK UMA (G4III-I, $\dot{M}_\star = 0.0077 \dot{M}_\odot/R_\odot^2$, $R_o \sim 2.51$).

We do not expect evolved stars to follow the same trend as unsaturated main sequence stars because their winds might be generated from a different mechanism (such as pulsations, see Vidotto 2021). As for 70 Oph A and B, we do not have much insight into their eruptive activity levels in order to rule out whether or not the \dot{M}_\star

inferred from the astrospheric technique was influenced by slingshot prominences or CME activity.

As can be seen in Fig. 6, our numerical results in this region are essentially bracketed by the observations for which the R_o reaches larger values. The largest Rossby number from our star sample corresponds to HD 219134 (K3V, $R_o = 2.02732$), which is comparable to the accepted solar value. Since our models use ZDI maps as inner boundary conditions to simulate stellar winds, this implies that extending our numerical models to even larger R_o would be very challenging as those ZDI reconstructions would require prohibitively long observing campaigns.

While we have limited data points, we see that for objects with $R_o \lesssim 0.15$, we do not obtain larger numerical values \dot{M}_\star even when the magnetic field strengths increase dramatically. For example, in the case of YZ CMi ($B_R^{\max} = 822$ G, $\dot{M}_\star/R_\star^2 = 20.57 \dot{M}_\odot/R_\odot^2$) and GJ 1245 B ($B_R^{\max} = 404$ G, $\dot{M}_\star = 9.27 \dot{M}_\odot/R_\odot^2$). All stars on the left-hand side of Fig. 6 lie beneath the maximum \dot{M}_\star value obtained for YZ CMi ($B_R^{\max} = 822$ G, $\dot{M}_\star/R_\star^2 = 20.57 \dot{M}_\odot/R_\odot^2$). This is true even when R_o varies by more than one dex, magnetic field strength by factors of 100, and the expected complexity number by ~ 4 .

These results indicate that the contribution from the steady wind will only account for a small fraction of the \dot{M}_\star budget in the case of very active stars. Furthermore, the obtained behaviour hints of a possible saturation of the steady-state stellar wind contribution to \dot{M}_\star , while the star could still lose significant mass through other mechanisms such as slingshot prominences or CME activity due to flares among others.

According to Villarreal D'Angelo et al. (2017) and references therein, cool stars can support prominences if their magnetospheres are within the centrifugal regime (i.e. $R_K < R_A$, where $R_K = \sqrt[3]{GM_\star/\Omega_\star^2}$ is the co-rotation radius). They provide estimates for the prominence masses (m_p) and the ejection time-scales (t_p) for a sample of cool stars. According to their analysis, DT Vir would have $m_p = 1.5 \times 10^{15}$ g and $t_p = 0.1$ d, while the values for GJ 1245 B would be $m_p = 4.4 \times 10^{14}$ g, $t_p = 0.3$ d. Using these values, they also reported the expected mass loss rate from prominences for these two stars in absolute units. In order to compare with the steady state wind, we convert their results to units of \dot{M}_\odot/R_\odot^2 . For DT Vir we have $\dot{M}_\star^p/R_\star^2 = 0.49 \dot{M}_\odot/R_\odot^2$ and for GJ 1245 B the resulting value is $\dot{M}_\star^p/R_\star^2 = 0.68 \dot{M}_\odot/R_\odot^2$.

For the CMEs contribution, we can obtain an order of magnitude estimate by following the approach in Odert et al. (2017). They estimate the mass-loss rate from the CME ($\dot{M}_\star^{\text{CME}}$) as a function of L_X and the power law index (α) of the flare frequency distribution. For the X-ray luminosity, we used the Liefke & Schmitt (2007) database, and for the flare frequency distribution exponent we took $\alpha = 2$ (Hawley et al. 2014).

For DT Vir, with $\log(L_X) = 29.75$, we obtain $\dot{M}_\star^{\text{CME}}/R_\star^2 \sim 160 \dot{M}_\odot/R_\odot^2$. For GJ 1245 B, with $\log(L_X) = 27.47$, the estimated CME-mass loss rate is $\dot{M}_\star^{\text{CME}}/R_\star^2 \sim 12.8 \dot{M}_\odot/R_\odot^2$.

We emphasize here that this approach assumes that the solar flare-CME association rate holds for very active stars (see the discussion in Drake et al. 2013). As such, it does not consider the expected influence due to CME magnetic confinement (e.g. Alvarado-Gómez et al. 2018, 2019) which currently provides the most suitable framework to understand the observed properties of stellar CME events and candidates (Moschou et al. 2019; Alvarado-Gómez et al. 2022a; Leitzinger & Odert 2022).

Still, we can clearly see that the input from CMEs to the total \dot{M}_\star could be higher than the steady wind and prominences for these two

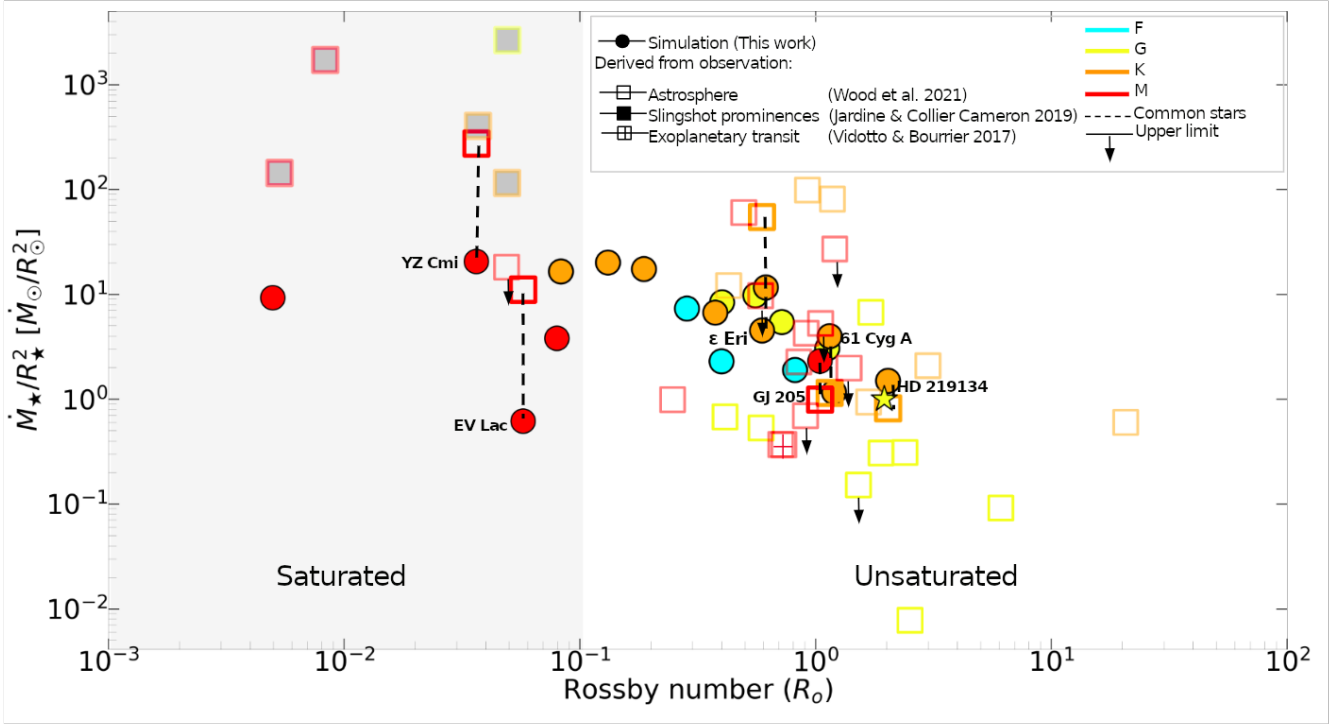


Figure 6. Numerical results of the stellar mass loss rate (\dot{M}_\star/R_\star^2 , circles), astrosphere stellar mass loss rate (squares, Wood et al. 2021), slingshot prominences mass loss rate (diamonds, Jardine & Collier Cameron 2019), and absorption during an exoplanetary transit (plus within a square, Vidotto & Bourrier 2017) against the Rossby number (R_o). Colors illustrate the different spectral types: cyan (F), yellow (G), orange (K), and red (M). The Sun is represented by a star symbol. Dashed lines connect the common stars between our sample and the ones with estimated \dot{M}_\star/R_\star^2 values by the astrospheric Ly- α absorption technique. Black arrows pointing downward correspond to the upper limits given by observations.

stars (with the latter contributing less in these cases). For instance, the estimated contribution of CMEs to the total \dot{M}_\star of DT Vir is almost 40 times higher than the value obtained for the steady stellar wind.

We will discuss the cases of EV Lac and YZ CMi in Section 3.3.2

3.3.1 Comparison between simulations and observations

In addition to analyzing the general trends, we can compare the models for common stars between our sample and the observations in Wood et al. (2021) and references therein. The stars in Wood et al. (2021) contain a total number of 37 stars with a mix of main-sequence and evolved stars. The sample includes 15 single K-G stars among them 4 evolved stars, and 4 binaries. Wood et al. (2021) reports individual \dot{M} values for the G-K binary pairs (this means that it was possible to model their individual contribution to the astrosphere of the system or they were separated enough not to share a common astrosphere). This is important as, in principle, one could treat the binary pairs as individual stars. The rest of the star sample includes 22 M-dwarfs with 18 single M-dwarfs, 3 binaries, and 1 triple system. Unlike the G-K stars, \dot{M}_\star values for the M-dwarf binaries/triple system are listed as a single value (therefore, it means that it has to be taken as the aggregate of all the stars in the system). For the binary system GJ 338 AB we were unable to include it in the plot of Fig. 6 due to a lack of needed information to estimate its R_o .

Following on the results from Sect. 3.3, our simulated mass loss rates for stars in the unsaturated regime agree well with those es-

timated from astrospheric detections (see Fig. 6). Specifically, for GJ 205 (M1.5V), 61 Cyg A (K5V), and HD 219134 (K3V) we obtain \dot{M}_\star/R_\star^2 of 2.32, 3.98, and 1.50, respectively. These values are all consistent with their respective observational estimates, taking into account the typical uncertainties of the astrospheric absorption method⁷. While further observations could help to confirm this, the agreement between our asynchronous models and the observations indicates that, within this R_o range, the temporal variability of \dot{M}_\star is minimal. This is certainly the case for the Sun ($R_o \sim 2.0$) in which long-term monitoring has revealed only minor variability of the solar wind mass loss rate over the course of the magnetic cycle (Cohen 2011, Finley et al. 2018, 2019).

On the other hand, \dot{M}_\star from the 3D MHD simulations appear to fall short by an order of magnitude or more from the available estimates for ϵ Eri (K2V), EV Lac (M3.5V), and YZ CMi (M4.5V) with \dot{M}_\star/R_\star^2 of 4.53, 0.62 and 20.57, respectively. We will discuss different possibilities for these discrepancies on each star in Sect. 3.3.2. However, it is important to remember that the \dot{M}_\star estimates from the Ly- α absorption technique contain systematic errors that are not easily quantified. One example is that they depend on the assumed properties and topology of the ISM (Linsky & Wood 2014), which have not been fully agreed upon in the literature (e.g., Koutroumpa et al. 2009; Gry & Jenkins 2014; Redfield & Linsky 2015). While studies

⁷ Astrospheric estimates on \dot{M}_\star should have an accuracy of about a factor of 2 with substantial systematic uncertainties (Wood et al. 2005b).

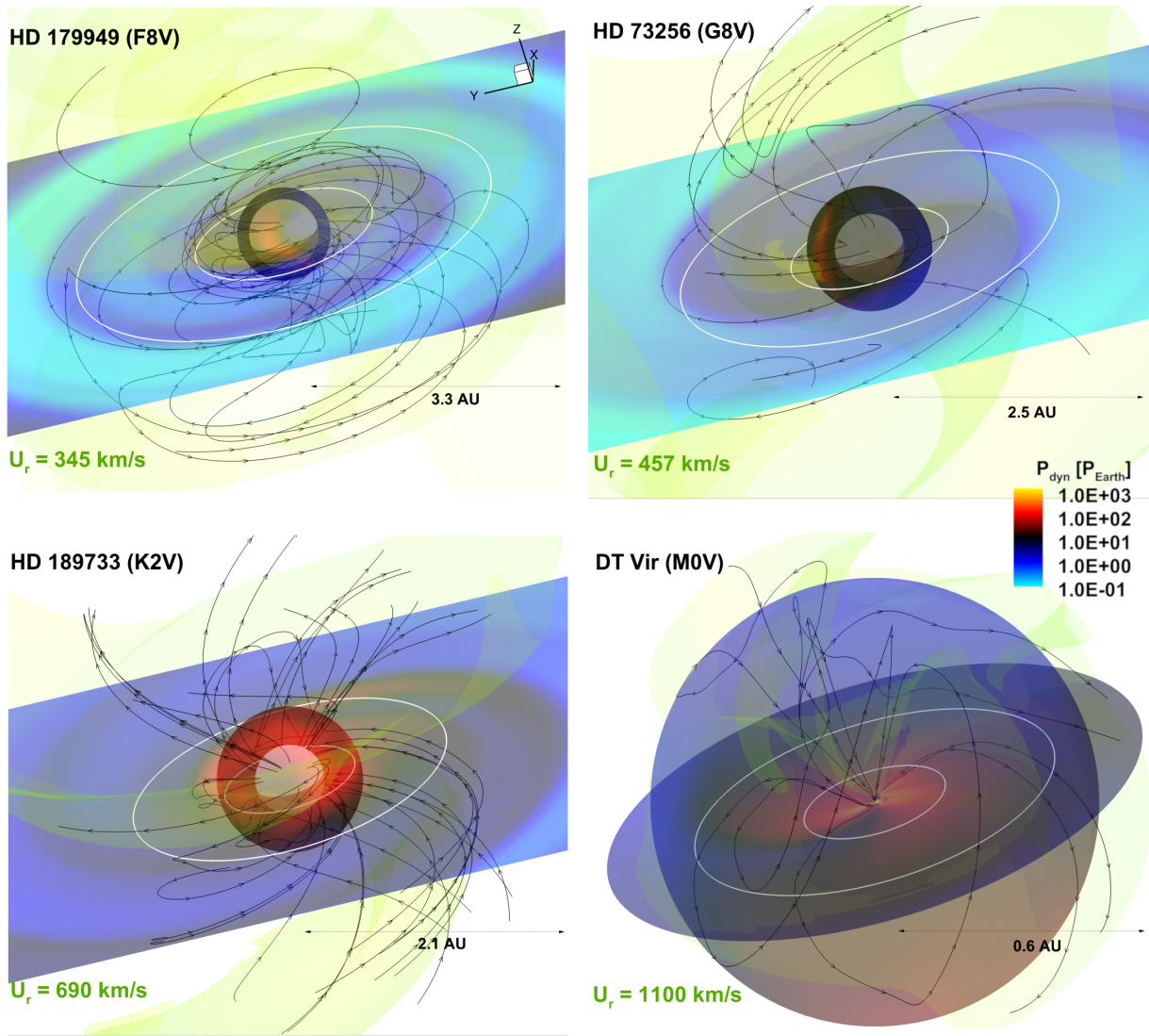


Figure 7. Simulated stellar wind environment for HD 179949, HD 73256, HD 189733, and DT Vir. Multi-domain models for HD 179949, HD 73256, HD 189733 are shown. The steady-state solution of the multi-domain cases is propagated from the coupling region ($62 - 67 R_{\star}$) to the entire IA domain ($1200 R_{\star}$ in each cartesian direction). The steady-state solution of DT Vir is shown in the spherical domain (SC). The green iso-surface represents the averaged wind velocity at 1 au for F, G, and K, as for M-dwarfs it represents the highest averaged velocity. Color-coded is the wind dynamic pressure ($P_{\text{dyn}} = \rho U^2$) normalized to the nominal Sun-Earth value (~ 1.5 nPa), visualized on the equatorial plane of both domains and on a translucent sphere (at $R = 0.5$ au). Selected magnetic field lines are shown in black. The 2 white circles represent the optimistic habitable zone boundaries. The white translucent sphere represents the coupling region ($67 R_{\star}$) between the SC and IH domains in the case of F, G, and K stars.

have provided a detailed characterization of the local ISM (see Redfield & Linsky 2008a; Redfield & Linsky 2015; Gry & Jenkins 2014), intrinsic uncertainties and additional observational limitations can greatly alter the estimated mass-loss rate values. These include column densities, kinematics, and metal depletion rates (Redfield & Linsky 2004a, 2008b), as well as local temperatures and turbulent velocities (Redfield & Linsky 2004b).

Furthermore, we would also like to emphasize the variation of the \dot{M}_{\star} in the astrospheric estimates with the assumed stellar wind velocity, as we believe that this factor is one of the largest potential source of uncertainty and discrepancy with our models. As discussed by Wood et al. (2021), this parameter is used as input in 2.5D hydrodynamic models to quantify the stellar wind mass loss rate. The Ly- α absorption signature, leading to \dot{M}_{\star} , is determined to first order by the size of the astrosphere. The latter depends on the stellar

wind dynamic pressure ($P_{\text{dyn}} \propto \dot{M}_{\star} U_{\text{sw}}$), which implies an inverse relation between \dot{M}_{\star} and \dot{U}_{sw} (Wood et al. 2002).

The astrospheric analysis of Wood et al. (2021) assumed a stellar wind velocity of 450 km s^{-1} at 1 au (matching models of the heliosphere) for all main-sequence stars. However, we find that stellar wind velocities can vary significantly between different types of stars and even among the same spectral type for different magnetic field strengths and rotation periods. To quantify this, we compute the average terminal velocity of the wind, ($\overline{U_R^T}$), by averaging U_R over a sphere extracted at 99% of the maximum extent of each simulation domain ($594 R_{\star}$ for F, G, and K stars and $248 R_{\star}$ for M-dwarfs; see Sect. 2). In the cases in which the spatial extension of our numerical domain allowed, we also computed the average wind velocity at 1 au. The resulting values, listed in Table 2, indicate variations in the wind velocity by factors of 5 or more when moving from F-type stars

Table 2. A summary of the resulting stellar wind properties with their corresponding driving parameters. Columns 1–11, list the star number, name, mass-loss rate per unit surface area[†] (\dot{M}_\star/R_\star^2), angular momentum loss rate (J_\star), average terminal velocity ($\overline{U}_R^{\text{1au}}$), average terminal velocity ($\overline{U}_R^{\text{T}}$), average Alfvén surface radius (\overline{AS}), absolute maximum surface radial magnetic field ($|B_R|^{\text{max}}$), average surface radial magnetic field (B_R^{avg}), Rossby number[‡] (R_o), and the expected complexity number[§] (n).

ID number	Name	\dot{M}_\star/R_\star^2	J_\star [g.cm ² .s ⁻¹]	$\overline{U}_R^{\text{1au}}$ [km s ⁻¹]	$\overline{U}_R^{\text{T}}$ [km s ⁻¹]	\overline{AS} [R _★]	$ B_R ^{\text{max}}$ [G]	B_R^{avg} [G]	R_o	n
1	τ Boo	2.30	1.35E+30	320	332	13	14	4.01	0.39855	1.84728
2	HD 179949	1.90	2.07E+29	345	356	11	12	3.91	0.81648	2.65746
3	HD 35296	7.33	1.20E+30	270	289	20	27	13.94	0.28396	1.63835
4	HN Peg	8.42	1.07E+30	545	549	16	50	20.48	0.40079	1.85148
5	HD 190771	5.45	2.58E+29	431	432	14	24	11.75	0.71806	2.46397
6	TYC 1987-509-1	9.82	2.11E+29	547	530	17	54	25.63	0.55388	2.14387
7	HD 73256	3.04	5.18E+28	457	458	11	22	7.91	1.12036	3.25857
8	HD 130322	1.17	8.01E+27	436	440	9	5	2.08	1.19721	3.41113
9	HD 6569	6.70	7.88E+28	704	702	18	29	18.41	0.37507	1.80346
10	ε Eri	4.53	6.89E+28	554	553	14	25	12.26	0.59172	2.21724
11	HD 189733	11.67	1.34E+29	535	534	16	51	28.43	0.61443	2.26141
12	HD 219134	1.50	4.97E+27	425	429	9	6	3.44	2.02732	5.06451
13	TYC 6878-0195-1	17.42	2.08E+29	734	692	24	162	60.14	0.18682	1.48069
14	61 Cyg A	3.98	7.98E+27	609	593	13	18	10.07	1.14548	3.30842
15	HIP 12545	20.11	2.13E+29	906	891	28	184	106.62	0.13145	1.41505
16	TYC 6349-0200-1	16.55	1.92E+29	657	642	23	93	51.36	0.08314	1.40684
17	DT Vir	3.81	2.67E+28	—	1102	37	327	125.08	0.07979	1.41024
18	GJ 205	2.32	2.28E+27	—	690	17	22	14.41	1.04304	3.10525
19	EV Lac	0.62	4.10E+26	—	3675	122	1517	620.21	0.05738	1.46331
20	YZ CMi	20.57	1.81E+28	—	1709	132	822	655.66	0.03637	1.62264
21	GJ 1245 B	9.27	1.90E+27	—	1164	44	404	200.43	0.00498	5.02602

[†] Normalized to solar units ($\dot{M}_\odot/R_\odot^2 = 1.0$).

[‡] Predicted by the empirical model of Wright et al. (2011a).

($\overline{U}_R^{\text{T}} \sim 325 \text{ km s}^{-1}$) to M-dwarf ($\overline{U}_R^{\text{T}} \sim 1500 \text{ km s}^{-1}$). This is also illustrated in Fig. 7, which portrays the simulated stellar wind environment for HD 179949 (F8V), HD 73256 (G8V), HD 189733 (K2V), and DT Vir (M0V). We include a green iso-surface that corresponds to the wind velocity at 1 au for F, G, and K stars as for M-dwarfs it represents the average terminal wind velocity in the domain. The visualizations also include the equatorial projection of the wind dynamic pressure ($P_{\text{dyn}} = \rho U^2$), normalized to the nominal Sun-Earth value, as well as on a sphere highlighting the wind 3D structure at 0.5 au.

What is clear from this analysis is that is not ideal to use the same wind velocity for all spectral types. Even within the same spectral type, we can observe a wide range of terminal velocities (e.g., the velocity in K stars ranges from 400 km s^{-1} to 700 km s^{-1}). As such, for models that require wind velocity as an input parameter, we recommend using the average radial wind velocity among a given spectral type.

For G-K stars, we obtain wind velocities at 1 au in the range of 400 to 700 km s^{-1} which is not too different from the wind velocity assumption of Wood et al. 2021. This is also consistent with the fact that for these spectral types, we have a better agreement between \dot{M} estimated from our simulations and those from the astrospheric technique (Wood et al. 2021). For lower mass stars with relatively small R_o we obtain velocities higher than 450 km s^{-1} up to 3675 km s^{-1} .

Note that due to computational limitations, the extent of our M-dwarf simulations does not reach up to 1 au (varying from 0.6 au for DT Vir to 0.16 au for GJ 1245 B). Nevertheless, as indicated by the calculated terminal velocities, even at closer distances the wind velocity is already $> 450 \text{ km s}^{-1}$, a situation that should still hold when propagated out to 1 au. Wind velocities on the order of 1000 – 1500 km s^{-1} at distances of 1 au and beyond had been reported in high-resolution AWSOM simulations of the environment around the M5.5V star Proxima Centauri (Alvarado-Gómez et al. 2020). This helps to explain why our simulated mass-loss rates for EV Lac, YZ CMi, and ε Eri were lower than the observed ones (differences larger than a factor of 2). We discuss these cases in more detail in the following section.

3.3.2 Exploring the cases of EV Lac, YZ CMi, ε Eri

(i) YZ CMi & EV Lac

Frequent stellar flares have been observed at YZ CMi in several wavelength ranges (Lacy et al. 1976; Mitra-Kraev et al. 2005; Kowalski et al. 2013; Bicz et al. 2022). The flaring energy distribution of this star ranges from $10^{30.6}$ to $10^{34.09} \text{ erg}$ (Bicz et al. 2022) with a total flaring time that varies from 21 to 306 minutes. Likewise, there is also significant flare activity on EV Lac (Leto et al. 1997; Muheki et al. 2020). From spectroscopic and photometric studies of EV Lac,

Muheki et al. (2020) reports to have found 27 flares (~ 5.0 flares per day) in H α with energies between 1.61×10^{31} erg – 1.37×10^{32} erg and 49 flares (~ 2.6 flares per day) from the TESS lightcurve with energies of 6.32×10^{31} erg – 1.11×10^{33} erg. With such high flare activity, it is possible that a large fraction of the \dot{M}_\star estimated in Wood et al. (2021) for these stars could arise from transient phenomena (e.g., prominences, CMEs).

Following the same approach described at the end of Section 3.3.1, we can obtain a rough estimate of \dot{M} from CMEs for EV Lac and YZ CMi. For EV Lac we find $\dot{M}_{\text{CME}}/R_\star^2 = 55.5 \dot{M}_\odot/R_\odot^2$ assuming $\log(L_X) = 28.69$. In the case of YZ CMi, an $\log(L_X) = 28.53$ yields $\dot{M}_{\text{CME}}/R_\star^2 = 47.6 \dot{M}_\odot/R_\odot^2$. However, given the magnetic field strength observed in EV Lac and YZ CMi (a few kG, Shulyak et al. 2010; Reiners et al. 2022; Cristofari et al. 2023), we expect that the magnetic confinement of CMEs would play an important role in these objects (see Alvarado-Gómez et al. 2019, Muheki et al. 2020, Maehara et al. 2021). Therefore, it is not straightforward to estimate exactly how large the contribution of CMEs to \dot{M}_\star is for these stars.

In addition, as discussed by Villarreal D’Angelo et al. (2017), EV Lac and YZ CMi are considered in the slingshot prominence regime. For EV Lac they estimate $m_p = 2.0 \times 10^{16}$ g and $t_p = 0.6$ d, while for YZ CMi values of $m_p = 4.5 \times 10^{16}$ g and $t_p = 0.6$ d are given. Using the associated mass loss rate values reported in Villarreal D’Angelo et al. (2017), we obtain $\dot{M}_p/R_\star^2 = 3.16 \dot{M}_\odot/R_\odot^2$ for EV Lac and $\dot{M}_p/R_\star^2 = 8.32 \dot{M}_\odot/R_\odot^2$ for YZ CMi.

This suggests another possible explanation for the discrepancies between our models and the astrospheric estimates is that some of the stellar wind detected for EV Lac and YZ CMi contains material from the slingshot prominences. Indeed, the location of the latter in the $\dot{M}_\star - R_\odot$ diagram (Fig. 6) appears more consistent with the mass loss rate estimates from slingshot prominences by Jardine & Collier Cameron (2019).

Moreover, Wood et al. (2021) noted that the YZ CMi astrospheric absorption comes primarily from neutrals near and inside the astropause, rather than from the hydrogen wall where neutral H density is highest. Therefore, using Ly alpha absorption to calculate \dot{M}_\star from YZ CMi will result in substantial uncertainty.

Finally, as mentioned in Sect. 3.3.1, there is a significant difference between the wind velocity assumed by Wood et al. (2021) and our results. Our average terminal wind velocity for YZ CMi (1709 km s^{-1}) and EV Lac (3675 km s^{-1}) is significantly higher than the wind velocity of 450 km s^{-1} assumed in Wood et al. (2021) at 1 au. While the wind velocity in EV Lac might be overestimated in our models (due to the usage of fiducial AWSoM parameters), we still expect relatively large wind velocities for this star ($\sim 1000 - 1500 \text{ km s}^{-1}$) given its magnetic field strength and Rossby number (see e.g., Kavanagh et al. 2021; Alvarado-Gómez et al. 2022b). As was discussed in Sect. 3.3.1, while our terminal wind velocity for M-dwarfs is calculated closer to the star (0.33 au for YZ CMi and 0.16 au for EV Lac), we do not expect a large reduction in the average velocity between these distances and 1 au. As such, the fast wind velocity resulting in our simulations of YZ CMi and EV Lac would imply lower \dot{M}_\star values when analyzed following the astrospheric technique of Wood et al. (2021).

(ii) ϵ Eri

With a relatively slow rotation period (11 d), and weak large-scale magnetic field (< 50 G), ϵ Eri cannot be considered within the slingshot prominence regime (like in the cases of YZ CMi and EV Lac). Because of this, we do not expect a significant presence of slingshot prominences in the \dot{M} value of this star. On the other hand, the analysis of Loyd et al. (2022), estimated the contribution of

flare-associated CMEs to the mass loss rate. They reported an upper limit of $1.09 \dot{M}_\odot/R_\odot^2$, which is insignificant when compared to the star’s overall estimated \dot{M}_\star value by Wood et al. (2021) and the astrospheric technique ($56 \dot{M}_\odot/R_\odot^2$). Therefore, the contribution from CMEs is also most likely not responsible for the elevated astrospheric \dot{M}_\star value on this star and its discrepancy with our steady-state models.

On the other hand, multiple observations of the large-scale magnetic field geometry of ϵ Eri reveal that it evolves over a time-scale of months (Jeffers et al. 2014; Jeffers et al. 2017). According to Jeffers et al. (2014), the maximum field strength can reach up to 42 G. As shown in Fig. 3, a global increase in the magnetic field strength causes an increase in \dot{M}_\star . The Zeeman Doppler Imaging map of ϵ Eri used to drive the 3D MHD model has a $B_R^{\text{max}} = 25$ G leading to $\dot{M}_\star/R_\star^2 = 4.53 \dot{M}_\odot/R_\odot^2$. This value is comparable to the numerical result obtained by Alvarado-Gómez et al. (2016) for this star ($\dot{M}_\star/R_\star^2 \sim 5.3 \dot{M}_\odot/R_\odot^2$). Increasing the surface magnetic field strength of ϵ Eri to the maximum value reported in observations will raise the mass loss rate to $\sim 10 \dot{M}_\odot/R_\odot^2$. As such, the variability of the stellar magnetic field and its expected modulation of the stellar wind properties could account for some of the differences between the simulated and the observed mass loss rates. However, corroborating this would require contemporaneous ZDI and astrospheric measurements which, to our knowledge, have not been performed on any star so far. As ϵ Eri goes through a magnetic/activity cycle (Metcalfe et al. 2013; Jeffers et al. 2017), we can expect relatively large variations in \dot{M}_\star values in our Alfvén-wave driven stellar wind models.

Finally and following the discussion for YZ CMi and EV Lac, the average wind velocity for ϵ Eri at 1 au (554 km s^{-1}) resulting from our models exceeds the one assumed in Wood et al. (2021). This will result in a smaller estimated \dot{M}_\star value from the pressure-balance astrospheric technique. In this way, the deviation between our models and the astrospheric detection of ϵ Eri could be due to the combined contribution of all the preceding elements (i.e., CMEs, cycle-related variability of the magnetic field, higher stellar wind velocity), and therefore we do not consider this discrepancy critical to our analysis.

3.4 Stellar wind and Circumstellar region

This section focuses on using the stellar wind results obtained from the 3D MHD simulations to assess the conditions an exoplanet would experience. This includes the characterization of the Alfvén surface for the various stellar wind solutions, the properties of the stellar wind in the habitable zone of these stars (in terms of the dynamical pressure of the wind), and the resulting magnetosphere size for these stellar wind conditions (assuming that a planet with the same properties/magnetization as Earth is in the HZ of these stars). The obtained quantities are listed in Table 2 and 3.

3.4.1 Stellar wind properties and orbital distances

(i) Alfvén surface size

Figure 8 summarizes our results showing the stellar wind environment around cool main sequence stars. We include the average size of the AS, resulting from our 21 3D MHD models, indicated in filled diamonds. To complement this information, empty diamonds correspond to the expected average AS size employing the scaling relation provided in Sect. 3.1, and using the ZDI information from 29 additional stars (See et al. 2019c and reference therein). The green region

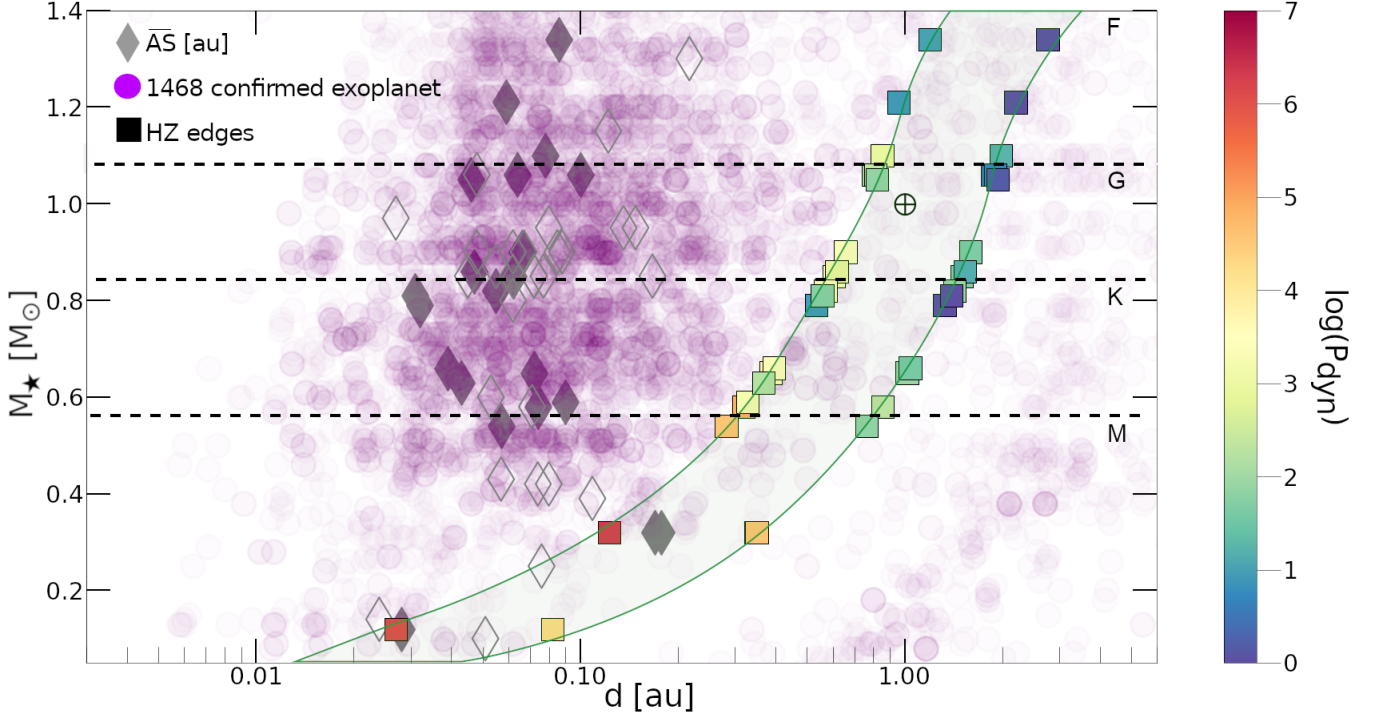


Figure 8. Numerical results of the average Alfvén surface size (diamonds), the inner and outer edge of the HZ (square, Kopparapu et al. 2014) derived using scaling laws that connect M_\star , R_\star , L_\star , and T_{eff} , against M_\star . The filled diamonds correspond to the \overline{AS} of the 21 stars in our sample. The empty diamonds are the \overline{AS} of other stars derived from our $\overline{AS} - B_R$ relation: $\log \overline{AS}_R = (0.42 \pm 0.06) \log B_R^{\text{avg}} + (0.71 \pm 0.07)$. The habitable zone boundaries are color-coded by the corresponding average dynamic pressure ($\overline{P}_{\text{dyn}}$) in logarithmic scale. The green shaded area represents the optimistic habitable zone. Earth is represented by \oplus . The purple circles correspond to some confirmed exoplanets (taken from the NASA exoplanet archive). The dynamic pressure at the outer edge of the HZ of DT Vir and GJ 205 (derived from scaling laws) is missing in the plot since it goes beyond the simulation domain that was initially established using the measured L_\star and T_{eff} (Table 1). The dashed lines separate the different spectral types.

corresponds to the optimistic HZ, calculated using the approach provided by Kopparapu et al. (2014) and the expected behaviour of the luminosity, temperature as a function of stellar mass on the main sequence (Kasting et al. 1993; Kopparapu et al. 2014; Ramirez 2018). Each square indicates the limits of the optimistic HZ for each star in our sample. These have been color-coded by the stellar wind dynamic pressure, normalized to the average Sun-Earth value. The position of the Earth is indicated by the \oplus symbol. In the background, a sample of the semi-major axis of some exoplanets is included.

There are a few noteworthy aspects of Fig. 8. First of all, the 3D MHD simulated \overline{AS} values (filled diamonds) do not show a clear trend with stellar mass. Instead, we see more or less similar \overline{AS} regardless of the spectral type of the star (Table 2). We see a similar behavior for stars whose \overline{AS} were extracted from the scaling relationship presented in Eq. 3 (empty diamonds). There is a significant scatter in the obtained distribution of \overline{AS} against M_\star , indicating that the intrinsic dependency with the surface magnetic field properties can in principle be replicated among multiple spectral types. However, we remind the reader that this result is also partly a consequence of our fixed choice for the base parameters of the corona and stellar wind solution (Sect. 2.1.3), which could in principle vary among different spectral types and activity stages (i.e. ages). As such, the generalization of the results presented here requires further investigation from both, observational constraints and numerical simulations.

We can also see that for late K and M-dwarfs, \overline{AS} reaches orbital distances comparable to their HZ limits. Examples of this from our

sample are GJ 1245 B ($\overline{AS} = 0.028$ au, $HZ_{\text{inner}} = 0.033$ au) and YZ CMi ($\overline{AS} = 0.178$ au, $HZ_{\text{inner}} = 0.09$ au). This situation has been also identified in previous case studies of stellar winds and exoplanets (e.g. Vidotto et al. 2013; Cohen et al. 2014; Garraffo et al. 2017).

The location of the HZ relative to the stellar Alfvén surface must be considered when studying the interactions between a star and a planet. A planet orbiting periodically or continuously within the AS region could be directly magnetically connected to the stellar corona, which could have catastrophic effects on atmospheric conservation (Cohen et al. 2014; Garraffo et al. 2017; Strugarek 2021). On the other hand, a planet with an orbit far outside this limit will be decoupled from the coronal magnetic field and interact with the stellar wind in a manner similar to the Earth (e.g. Cohen et al. 2020; Alvarado-Gómez et al. 2020). In the case of a planet orbiting in and out of the AS, the planet will experience strongly varying wind conditions, whose magnetospheric/atmospheric influence will be greatly mediated by the typical time-scale of the transition (Harbach et al. 2021).

(ii) Dynamic pressure

We also see a general trend in Fig. 8 in which the dynamic pressure at the HZ boundaries increases as we move from earlier to later spectral types. For example, $\overline{P}_{\text{dyn}}^{\text{Inn,HZ}}$ for the lowest-mass star GJ 1245 B is $447.39 P_\oplus$ nearly 200 times stronger than for the highest-mass star τ Boo with $\overline{P}_{\text{dyn}}^{\text{Inn,HZ}} = 2.76 P_\oplus$. Our results also show a large variability in $\overline{P}_{\text{dyn}}$ as we move from the inner to the outer edge of the HZ of G, K, and M-dwarfs (Table 3). For these stars, the $\overline{P}_{\text{dyn}}$ at

Table 3. Numerical results of different parameters in our sample at the habitable zone. Columns 1–8, respectively, list the star name, average dynamic pressure at the middle of the HZ ($\overline{P}_{\text{dyn,HZ}}$), average dynamic pressure at the inner boundary of the HZ ($\overline{P}_{\text{dyn}}^{\text{Inn,HZ}}$), average dynamic pressure at the outer boundary of the HZ ($\overline{P}_{\text{dyn}}^{\text{Out,HZ}}$), the average magnetopause standoff radius ($\overline{R}_{\text{M,HZ}}$), the inner habitable zone (HZ_{inner}), the outer habitable zone (HZ_{outer}), the average equatorial Alfvén surface ($\overline{AS}_{\text{eq}}$). The habitable zones listed in this table were inferred using the measured L_{\star} and T_{eff} of each star in our sample (Table 1).

Name	$\overline{P}_{\text{dyn,HZ}}$ [P_{\oplus}]	$\overline{P}_{\text{dyn}}^{\text{Inn,HZ}}$ [P_{\oplus}]	$\overline{P}_{\text{dyn}}^{\text{Out,HZ}}$ [P_{\oplus}]	$\overline{R}_{\text{M,HZ}}$ [R_{E}]	HZ_{inner} [au]	HZ_{outer} [au]	$\overline{AS}_{\text{eq}}$ [R_{\star}]
τ Boo	1.02	2.76	0.40	7.85	1.253	2.901	9.99
HD 179949	0.92	2.51	0.48	7.99	0.983	2.294	10.24
HD 35296	2.93	7.77	1.48	6.58	0.925	2.157	12.78
HN Peg	6.74	18.58	3.47	5.73	0.812	1.904	13.65
HD 190771	3.96	11.01	2.02	6.26	0.744	1.748	12.35
TYC 1987-509-1	10.21	28.49	5.20	5.30	5.35	1.299	15.47
HD 73256	2.32	6.45	1.18	6.85	0.648	1.539	10.73
HD 130322	0.91	2.56	0.46	8.00	0.542	1.291	8.12
HD 6569	10.77	30.21	5.46	5.30	0.466	1.11	16.25
ϵ Eri	6.45	18.16	3.23	5.77	0.426	1.024	13.64
HD 189733	13.56	38.82	6.88	5.10	0.458	1.108	13.4
HD 219134	2.01	5.81	1.01	7.01	0.410	0.996	8.33
TYC 6878-0195-1	13.42	39.39	6.71	5.11	0.713	1.751	23.16
61 Cyg A	10.06	29.47	5.01	5.36	0.308	0.754	11.93
HIP 12545	20.28	60.51	9.98	4.77	0.509	1.267	24.45
TYC 6349-0200-1	13	40	6	5.14	0.443	1.116	21
DT Vir	31.48	88.97	16.20	4.43	0.191	0.486	29.24
GJ 205	9.73	29.65	4.73	5.39	0.201	0.517	15.91
EV Lac	12.15	33.18	6.27	—	0.094	0.245	119.16
YZ CMi	193.85	566.34	97.08	—	0.09	0.237	75.23
GJ 1245 B	140.89	447.39	68.15	—	0.033	0.087	38.12

the inner HZ is almost 6 times stronger than that at the outer edge of the HZ (i.e., EV Lac $\overline{P}_{\text{dyn}}^{\text{Inn,HZ}} = 33.18 P_{\oplus}$, $\overline{P}_{\text{dyn}}^{\text{Out,HZ}} = 6.27 P_{\oplus}$). For F stars, the difference is smaller, around a factor of 2 like in the case of HD 179949, where $\overline{P}_{\text{dyn}}^{\text{Inn,HZ}} = 2.51 P_{\oplus}$ and $\overline{P}_{\text{dyn}}^{\text{Out,HZ}} = 0.48 P_{\oplus}$. The reason is that the HZs of these stars are farther from the star, where the wind density starts to become less variable.

Moreover, in some cases, we have $\overline{P}_{\text{dyn}}$ at the inner and outer edge of the star HZ comparable to the typical range experienced by the Earth (0.75 and 7 nPa, Ramstad & Barabash 2021). For example, HD 73256 (G8V, 6.45 - 1.18 P_{\oplus} ~ 9.675 - 1.77 nPa), HD 130322 (K0V, 2.56 - 0.46 P_{\oplus} ~ 3.84 - 0.69 nPa), τ Boo (F7V, 2.76 - 0.40 P_{\oplus} ~ 4.14 - 0.6 nPa). For the case of M-dwarfs, we have dynamic pressures higher than those experienced by Earth, as in the case of DT Vir (M0V, 88.97 - 16.20 P_{\oplus} ~ 133.455 - 24.3 nPa). This is because the HZ is located near the star where the density is highest. This indicates that planets orbiting at very close distance to the star (~ 0.03 - 0.05 au) would experience extreme space weather conditions with P_{dyn} up to 10^3 and $10^4 P_{\oplus}$. These values are comparable

to the ones estimated in Alvarado-Gómez et al. (2020) for Proxima d and for Proxima b in Garraffo et al. (2016). However, the reader is reminded here that any point from our simulations should be interpreted as an indication of the average conditions, but should not be treated as a specific absolute value (since it will change depending on the instantaneous local density and velocity of the wind (both a function of the evolving stellar magnetic field).

In addition, we notice a scatter in $\overline{P}_{\text{dyn}}$ estimates at the HZ when comparing stars of the same spectral type. This is not surprising since the P_{dyn} depends on the wind velocity and density at a given place. This also translates into having a range of dynamic pressure that a planet will experience within the HZ. This will defer from one orbital distance to the other as we can see in Fig. 7 where we show the equatorial plane color-coded by the dynamic pressure.

We can use our 3D models to investigate also the influence due to the orbital inclination. To illustrate this, Fig. 9 shows a 2D projection of the normalized dynamic pressure P_{dyn} extracted from spherical surfaces matching the midpoint of the HZ of HD 179949 (F8V), TYC 198-509-1 (G7V), 61 Cyg A (K6V), and GJ 205 (M1.5V).

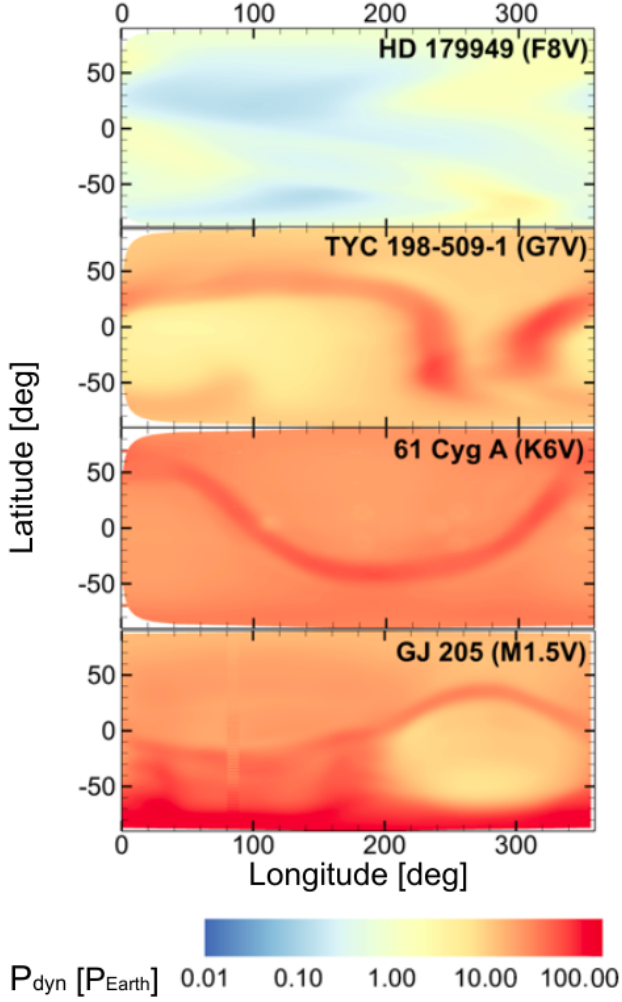


Figure 9. Two-dimensional Mercator projections of the normalized stellar wind dynamic pressure (P_{dyn}) extracted from the 3D MHD models of four stars in our sample covering F to M spectral types (HD 179949, TYC 198-509-1, 61 Cyg A, and GJ 205). Each P_{dyn} distribution was extracted from a spherical surface located at the midpoint habitable zone of each star.

We notice that in the case of F and G stars (i.e., HD 179949, and TYC-198-509-1) we have a large P_{dyn} variation with inclination around a factor 7. However, P_{dyn} values, are still relatively small in terms of absolute units (i.e., $0.01 - 10 P_{\oplus} \sim 0.015 - 15 \text{ nPa}$). For K and M-dwarfs, we see less variability in the P_{dyn} for the different inclinations, a more homogeneous P_{dyn} , especially in the case of the K star. However, in these cases, the P_{dyn} can reach values $> 100 P_{\oplus}$ ($> 150 \text{ nPa}$). Our results also show that even with an extreme orbit around the G-type star (TYC 198-509-1) with an inclination matching the current sheet, we would most likely not reach the very high P_{dyn} values as in the case of the K and M-dwarfs as we move closer to the star. As such, the inclination of the orbit plays a secondary role compared to the distance. This is clearly seen in the color gradient that gets redder and redder as we move toward lower masses (so the HZ is closer).

On the other hand, the variability of P_{dyn} , which we can see in Fig. 8 while represented in the same ‘spatial scale’, it does not coincide in terms of ‘temporal scales’. In other words, the x -axis in Fig. 8 do not correspond to the same timescale units for each star, where the

360 degrees of longitude correspond to “1 orbital period”. However, the orbital period is very different for a planet in the HZ of an F-type star (within a few au) compared to a planet orbiting an M-dwarf (within a fraction of an au). A planet orbiting an M-dwarf star experiences the variations in P_{dyn} on a much faster timescale (~ 1 day for each current sheet crossing), while these variations are much longer for more massive stars. This means that even if the P_{dyn} values were the same, the faster variability over the orbital period for low-mass stars would result in planets and their magnetospheres/atmospheres having less time to recover from passing through regions of high P_{dyn} than planets around more massive stars.

Finally, following the results compiled by Ramstad & Barabash (2021), if we consider the presence of a rocky exoplanet with an atmosphere similar to those of Venus and Mars at those mid-HZ locations, we would expect atmospheric ion losses between $2 \times 10^{24} \text{ ions s}^{-1}$ and $5 \times 10^{24} \text{ ions s}^{-1}$. This of course assumes that all processes occur in the same way as in the solar system (which might not be necessarily true for some regions of the vast parameter space of this problem). The ion losses will depend heavily on the type of stars that the exoplanet orbits, both in terms of the high-energy spectra and the properties of the stellar wind (see e.g. Egan et al. 2019a; France et al. 2020). If the rocky exoplanet is found around the HZ of an M-dwarf, the planet might suffer from unstable stellar wind conditions as previously stated that might increase the ion losses in the exoplanetary atmosphere. We will consider the case of Earth with its magnetosphere in the following section.

3.4.2 Magnetopause Standoff Distances

Using the dynamic pressure, we can define a first-order approximation to determine the magnetosphere standoff distance (R_M) of a hypothetical Earth-like planet orbiting at the HZ around each star in our sample. This is done by considering the balance between the stellar wind dynamic pressure and the planetary magnetic pressure (Eq. 8, Gombosi 2004; Shields et al. 2016):

$$R_M = R_E \left[\frac{B_p^2}{8\pi P_{\text{dyn}}} \right]^{\frac{1}{6}} \quad (8)$$

The Earth’s equatorial dipole field and radius are represented by B_p and R_E respectively. Normally the total wind pressure should be considered (i.e., thermal, dynamic, and magnetic), but in all the cases here considered, we can neglect the contributions of the magnetic and thermal pressures. For this calculation, we assume an equatorial dipole magnetic field of 0.3 G, similar to that of the Earth (Pulkkinen 2007). The magnetospheric standoff distance is expressed in Earth’s radii (Eq. 8). The different $\bar{R}_{M,\text{HZ}}$ values for the different stars in our sample are listed in table 3. Note that we only estimate the R_M in the cases where the HZ is in the super-Alfvénic regime (Cohen et al. 2014; Strugarek 2018).

Our estimated $R_{M,\text{HZ}}$ for F, G, and early K stars have values closer to the standard size of Earth’s dayside magnetosphere ($\sim 10 R_{\oplus}$, see Pulkkinen 2007; Lugaz et al. 2015). This is comparable to the value obtained by Alvarado-Gómez et al. (2020) for Proxima c ($\sim 6 - 8 R_{\oplus}$ in both activity levels), assuming an Earth-like dipole field on the planet surface. For the late K and M-dwarfs in our star sample, R_M starts to reach lower values $< 50\%$ from that of Earth. This suggests that a planet orbiting these stars must have a stronger dipole magnetic field than that of the Earth to withstand the wind conditions since $R_M \propto B_p^{1/3}$. However, in Ramstad & Barabash (2021) they show that contrary to what we have seen so far, the magnetosphere might

actually not act as a shield for the stellar wind-driven escape of planetary atmospheres. In fact, they reported an ion loss for Earth that ranges from 6×10^{24} ions s^{-1} - 6×10^{26} ions s^{-1} which is higher than what Venus and Mars lose. Further modeling studies are needed in order to characterize the stellar wind influence on the atmospheric loss of rocky exoplanets (e.g., Egan et al. 2019b; France et al. 2020), whose input stellar wind parameters can be extracted from this investigation.

4 SUMMARY & CONCLUSIONS

In this study we employed a state-of-the-art 3D MHD model (SWMF/AWSOM) to investigate the dependencies between different star properties (R_{\star} , M_{\star} , B_R , and P_{rot}) and a number of stellar wind parameters (AS, \dot{M}_{\star} , J_{\star} , P_{dyn}) of cool main sequence stars. We present numerical results of 21 stars going from F to M stars with magnetic field strengths between 5 and 1.5 kG and rotation periods between 0.71 d and 42.2 d. The large-scale magnetic field distribution of these stars, obtained by previous ZDI studies, were used to drive the solutions in the Stellar Corona domain, which are then self-consistently coupled for a combined solution in the Inner Astrosphere domain in the case of F, G, and K stars.

Our results showed a correlation between the average AS size and B_R^{avg} , regardless of the spectral type of the star (Eq. 3). We also obtained a strong correlation between \dot{M}_{\star} and B_R^{avg} for the different spectral types (excluding EV Lac, Eq. 4). The correlation between J_{\star} and B_R , on the other hand, was dominated by the absolute dependence on the stellar size, with significant scatter resulting mainly from the variability in \dot{M}_{\star} , the distribution of Ω_{\star} in our sample and the equatorial AS size where the maximum torque is applied.

Having established these star-wind relations, we looked in detail at \dot{M}_{\star} , since it is the only observable parameter of the stellar wind for which comparisons can be made. Using the complexity number as a function of the Rossby number R_o —defined previously in the literature—we were able to investigate the dependence of magnetic complexity on \dot{M}_{\star} . Our results showed that for more active stars, as in the case of M-dwarfs, the field strength starts to dominate over the complexity in the contribution on shaping \dot{M}_{\star} . Also, for cases in which the magnetic field strength and complexity were comparable, we obtained similar \dot{M}_{\star} . This indicates that in these cases the stellar properties (R_{\star} , M_{\star} , and P_{rot}) play a secondary role in changing \dot{M}_{\star} .

We then used our stellar wind results to investigate its behaviour with respect to the well-known stellar activity relationship (F_X vs R_o with the saturated and unsaturated regimes). For stars in the unsaturated regime, we see a trend where \dot{M}_{\star} increases with decreasing R_o (Eq. 7). For stars in the saturated regime, we find that the contribution of the steady wind is only a small part of the \dot{M}_{\star} budget. This suggests that there could be saturation in \dot{M}_{\star} due to the steady stellar wind, while the star could lose even more mass through other mechanisms, such as transient events (i.e. prominences, coronal mass ejections).

In addition to analyzing the general trends, we compared the model results of stars in our sample and objects with astrospheric \dot{M}_{\star} constraints. Our simulated \dot{M}_{\star} for stars in the unsaturated regime agree well with those estimated from astrospheric detections (namely for GJ 205, 61 Cyg A, and HD 219134). On the other hand, \dot{M}_{\star} from the 3D MHD simulations appear to differ by an order of magnitude or more from available estimates for ϵ Eri, EV Lac, and YZ CMi. We discussed how these results might be connected with the underlying assumption made by the observational analysis with respect to the

stellar wind speed. Indeed, for all the stars in which our models differed largely from the literature estimates, we obtained much larger stellar wind speeds than the ones used in the astrospheric method. As such, we emphasized the importance of using the appropriate wind velocity when estimating \dot{M}_{\star} from observations.

We further discussed various possibilities for the discrepancies in EV Lac, YZ CMi, ϵ Eri. For the two flaring stars, EV Lac and YZ CMi, we suspect that the high \dot{M}_{\star} estimates from the Ly- α absorption technique could be dominated by material from slingshot prominences and possibly CMEs (uncertain due to the expected magnetic confinement of CMEs in these stars). Note that this possibility was also considered by Wood et al. (2021) in the original astrospheric analysis. In the case of ϵ Eri, we do not expect a large contribution from prominences or CMEs to the observed \dot{M}_{\star} . However, as ϵ Eri undergoes a magnetic cycle, the stellar magnetic field and its expected modulation of stellar wind properties could explain some of the differences between the simulated and observed \dot{M}_{\star} .

Moreover, we used the stellar wind results from the 3D MHD simulations to assess the conditions that an exoplanet would experience, and provide the stellar wind conditions in the entire classical Habitable Zones of our target stars. Our results show a scatter in the obtained distribution of AS versus M_{\star} , suggesting that the intrinsic dependence with the surface magnetic field properties can be reproduced for several spectral types. With respect to the stellar wind dynamic pressure, our results show that the orbital inclination plays a secondary role compared to the orbital distance. We have also found that a planet orbiting K and M stars must have a stronger dipole magnetic field than that of Earth to withstand the wind conditions, if the planetary magnetic field is indeed acting as a shield (this paradigm, however, is starting to be challenged by solar system observations).

Finally, the properties of the stellar wind in the HZ of different spectral types obtained here can be used in future studies to, for instance, estimate the expected radio emission due to wind-magnetosphere interactions or the planetary atmospheric mass loss due to erosion of the stellar wind from ion escape processes.

ACKNOWLEDGEMENTS

The authors would like to thank the referee for valuable comments that improved the quality of the paper. The authors gratefully acknowledge the Gauss Centre for Supercomputing e.V. (www.gauss-centre.eu) for funding this project by providing computing time on the GCS Supercomputer SuperMUC-NG at Leibniz Supercomputing Centre (www.lrz.de) under application ID 21761 (PI: Alvarado-Gómez). JJC and KP acknowledge funding from the German *Leibniz Community* under project number P67/2018. CG was supported by NASA contract NAS8-03060 to the Chandra X-ray Center. This research has made use of NASA's Astrophysics Data System Bibliographic Services.

5 DATA AVAILABILITY

The data would be made available to the community on reasonable request due to the volume of the 3D simulations. Extractions of specific quantities discussed in the paper could be requested from the corresponding author.

REFERENCES

Ahuir J., Brun A. S., Strugarek A., 2020, *A&A*, **635**, A170

- Airapetian V. S., Gloer A., Khazanov G. V., Loyd R. O. P., France K., Sojka J., Danchi W. C., Liemohn M. W., 2017, *ApJ*, **836**, L3
- Alvarado-Gómez J. D., et al., 2015, *A&A*, **582**, A38
- Alvarado-Gómez J. D., Hussain G. A. J., Cohen O., Drake J. J., Garraffo C., Grunhut J., Gombosi T. I., 2016, *A&A*, **594**, A95
- Alvarado-Gómez J. D., Drake J. J., Cohen O., Moschou S. P., Garraffo C., 2018, *ApJ*, **862**, 93
- Alvarado-Gómez J. D., Drake J. J., Moschou S. P., Garraffo C., Cohen O., NASA LWS Focus Science Team: Solar-Stellar Connection Yadav R. K., Frascchetti F., 2019, *ApJ*, **884**, L13
- Alvarado-Gómez J. D., Drake J. J., Garraffo C., Cohen O., Poppenhaeger K., Yadav R. K., Moschou S. P., 2020, *ApJ*, **902**, L9
- Alvarado-Gómez J. D., Drake J. J., Cohen O., Frascchetti F., Garraffo C., Poppenhäger K., 2022a, *Astronomische Nachrichten*, **343**, e10100
- Alvarado-Gómez J. D., et al., 2022b, *ApJ*, **928**, 147
- Aschwanden M., 2006, *Physics of the Solar Corona: An Introduction with Problems and Solutions*. Springer Praxis Books, Springer Berlin Heidelberg, https://books.google.de/books?id=W7FE5_aowEQC
- Bicz K., Falewicz R., Pietras M., Siarkowski M., Preś P., 2022, *ApJ*, **935**, 102
- Biermann L., 1957, *The Observatory*, **77**, 109
- Boro Saikia S., Jin M., Johnstone C., Lüftinger T., Güdel M., Airapetian V., Kislyakova K., Folsom C., 2020a, *Astronomy & Astrophysics*, **635**
- Boro Saikia S., Jin M., Johnstone C. P., Lüftinger T., Güdel M., Airapetian V. S., Kislyakova K. G., Folsom C. P., 2020b, *A&A*, **635**, A178
- Charbonneau P., 2020, *Living Reviews in Solar Physics*, **17**, 4
- Chebly J. J., Alvarado-Gómez J. D., Poppenhaeger K., 2021, arXiv e-prints, p. arXiv:2111.09707
- Cohen O., 2011, *MNRAS*, **417**, 2592
- Cohen O., Drake J. J., Kashyap V. L., Sokolov I. V., Gombosi T. I., 2010, *ApJ*, **723**, L64
- Cohen O., Drake J. J., Gloer A., Garraffo C., Poppenhaeger K., Bell J. M., Ridley A. J., Gombosi T. I., 2014, *ApJ*, **790**, 57
- Cohen O., Garraffo C., Moschou S.-P., Drake J. J., Alvarado-Gómez J. D., Gloer A., Frascchetti F., 2020, *ApJ*, **897**, 101
- Cranmer S. R., 2012, *Space Sci. Rev.*, **172**, 145
- Cranmer S. R., Asgari-Targhi M., Miralles M. P., Raymond J. C., Strachan L., Tian H., Woolsey L. N., 2015, *Philosophical Transactions of the Royal Society of London Series A*, **373**, 20140148
- Cristofari P. I., et al., 2023, *MNRAS*, **522**, 1342
- Donati J.-F., et al., 2006, *Monthly Notices of the Royal Astronomical Society*, **370**, 629
- Drake S. A., Simon T., Brown A., 1993, *ApJ*, **406**, 247
- Drake J. J., Cohen O., Yashiro S., Gopalswamy N., 2013, *ApJ*, **764**, 170
- Egan H., Jarvinen R., Brain D., 2019a, *MNRAS*, **486**, 1283
- Egan H., Jarvinen R., Ma Y., Brain D., 2019b, *Monthly Notices of the Royal Astronomical Society*, **488**, 2108
- Evensberget D., Carter B. D., Marsden S. C., Brookshaw L., Folsom C. P., Salmeron R., 2022, *MNRAS*, **510**, 5226
- Fares R., et al., 2009, *MNRAS*, **398**, 1383
- Feldman W. C., 1977, *J. Geophys. Res.*, **82**, 667
- Fichtinger B., Güdel M., Mutel R. L., Hallinan G., Gaidos E., Skinner S. L., Lynch C., Gayley K. G., 2017, *A&A*, **599**, A127
- Finley A. J., Matt S. P., See V., 2018, *ApJ*, **864**, 125
- Finley A. J., See V., Matt S. P., 2019, *ApJ*, **876**, 44
- France K., et al., 2020, *AJ*, **160**, 237
- Gaidos E. J., Güdel M., Blake G. A., 2000, *Geophys. Res. Lett.*, **27**, 501
- Gallet F., Bouvier J., 2013, *A&A*, **556**, A36
- Gallet F., Bouvier J., 2015, *A&A*, **577**, A98
- Garraffo C., Drake J. J., Cohen O., 2015a, *ApJ*, **807**, L6
- Garraffo C., Drake J. J., Cohen O., 2015b, *ApJ*, **813**, 40
- Garraffo C., Drake J. J., Cohen O., 2016, *ApJ*, **833**, L4
- Garraffo C., Drake J. J., Cohen O., Alvarado-Gómez J. D., Moschou S. P., 2017, *ApJ*, **843**, L33
- Garraffo C., et al., 2018, *ApJ*, **862**, 90
- Garraffo C., Alvarado-Gómez J. D., Cohen O., Drake J. J., 2022, *ApJ*, **941**, L8
- Gastine T., Morin J., Duarte L., Reiners A., Christensen U. R., Wicht J., 2013, *A&A*, **549**, L5
- Gombosi T. I., 2004, *Physics of the Space Environment*. Cambridge University Press
- Gombosi T. I., van der Holst B., Manchester W. B., Sokolov I. V., 2018, *Living Reviews in Solar Physics*, **15**, 4
- Gombosi T. I., et al., 2021, *Journal of Space Weather and Space Climate*, **11**, 42
- Gry C., Jenkins E. B., 2014, *A&A*, **567**, A58
- Güdel M., Guinan E. F., Skinner S. L., 1997, *ApJ*, **483**, 947
- Gurnett D., Kurth W., 2019, *Nature Astronomy*, **3**
- Hansteen V. H., Velli M., 2012, *Space Sci. Rev.*, **172**, 89
- Harbach L. M., Moschou S. P., Garraffo C., Drake J. J., Alvarado-Gómez J. D., Cohen O., Frascchetti F., 2021, *ApJ*, **913**, 130
- Hawley S. L., Davenport J. R. A., Kowalski A. F., Wisniewski J. P., Hebb L., Deitrick R., Hilton E. J., 2014, *ApJ*, **797**, 121
- Hussain G. A. J., et al., 2016, *A&A*, **585**, A77
- Jardine M., Collier Cameron A., 2019, *MNRAS*, **482**, 2853
- Jeffers S. V., Petit P., Marsden S. C., Morin J., Donati J. F., Folsom C. P., 2014, *A&A*, **569**, A79
- Jeffers S. V., Boro Saikia S., Barnes J. R., Petit P., Marsden S. C., Jardine M. M., Vidotto A. A., the BCool collaboration 2017, *Monthly Notices of the Royal Astronomical Society: Letters*, **471**, L96
- Jivani A., et al., 2023, *Space Weather*, **21**, e2022SW003262
- Johnstone C. P., Güdel M., Lüftinger T., Toth G., Brott I., 2015a, *A&A*, **577**, A27
- Johnstone C. P., Güdel M., Brott I., Lüftinger T., 2015b, *A&A*, **577**, A28
- Jordan C., Montesinos B., 1991, *Monthly Notices of the Royal Astronomical Society*, **252**, 21P
- Kasper J. C., et al., 2021, *Phys. Rev. Lett.*, **127**, 255101
- Kasting J. F., Whitmire D. P., Reynolds R. T., 1993, *Icarus*, **101**, 108
- Kavanagh R. D., Vidotto A. A., Klein B., Jardine M. M., Donati J.-F., Ó Fionnagáin D., 2021, *MNRAS*, **504**, 1511
- Kislyakova K. G., et al., 2014, *A&A*, **562**, A116
- Klimchuk J. A., 2015, *Philosophical Transactions of the Royal Society of London Series A*, **373**, 20140256
- Kochukhov O., 2020, in Wade G., Alecian E., Bohlender D., Sigut A., eds, Vol. 11, *Stellar Magnetism: A Workshop in Honour of the Career and Contributions of John D. Landstreet*. pp 89–101 (arXiv:1912.07241), doi:10.48550/arXiv.1912.07241
- Kopparapu R. K., Ramirez R. M., SchottelKotte J., Kasting J. F., Domagal-Goldman S., Eymet V., 2014, *The Astrophysical Journal*, **787**, L29
- Koutroumpa D., Lallement R., Raymond J. C., Kharchenko V., 2009, *ApJ*, **696**, 1517
- Kowalski A. F., Hawley S. L., Wisniewski J. P., Osten R. A., Hilton E. J., Holtzman J. A., Schmidt S. J., Davenport J. R. A., 2013, *ApJS*, **207**, 15
- Lacy C. H., Moffett T. J., Evans D. S., 1976, *The Astrophysical Journal Supplement Series*, **30**, 85
- Leitzinger M., Odert P., 2022, *Serbian Astronomical Journal*, **205**, 1
- Leto G., Pagano I., Buemi C., Rodono M., 1997, *VizieR Online Data Catalog*, pp J–A+
- Liefke C., Schmitt J. H. M. M., 2007, *NEXXUS 2 - The Database for Nearby X-Ray and Extreme UV emitting Stars*, <https://hsweb.hs.uni-hamburg.de/projects/nexus/index.html>
- Lim J., White S. M., 1996, *The Astrophysical Journal Letters*, **462**, L91
- Linsky J. L., Wood B. E., 2014, *ASTRA Proceedings*, **1**, 43
- Loyd R. O. P., et al., 2022, *ApJ*, **936**, 170
- Lugaz N., Farrugia C., Huang C.-L., Spence H., 2015, *Geophysical Research Letters*, **42**
- Maehara H., et al., 2021, *PASJ*, **73**, 44
- Matt S. P., MacGregor K. B., Pinsonneault M. H., Greene T. P., 2012, *ApJ*, **754**, L26
- McComas D., et al., 1998, *Geophysical Research Letters*, **25**, 1
- McComas D. J., Elliott H. A., Schwadron N. A., Gosling J. T., Skoug R. M., Goldstein B. E., 2003, *Geophys. Res. Lett.*, **30**, 1517
- Metcalfe T. S., et al., 2013, *ApJ*, **763**, L26
- Mitra-Kraev U., et al., 2005, *Astronomy & Astrophysics*, **431**, 679
- Morin J., et al., 2008, *MNRAS*, **390**, 567
- Morin J., Donati J. F., Petit P., Delfosse X., Forveille T., Jardine M. M., 2010, *MNRAS*, **407**, 2269

- Moschou S.-P., Drake J. J., Cohen O., Alvarado-Gómez J. D., Garraffo C., Frascchetti F., 2019, *ApJ*, **877**, 105
- Muhéki P., Guenther E. W., Mutabazi T., Jurua E., 2020, *MNRAS*, **499**, 5047
- Noyes R. W., Hartmann L. W., Baliunas S. L., Duncan D. K., Vaughan A. H., 1984, *ApJ*, **279**, 763
- Odert P., Leitzinger M., Hanslmeier A., Lammer H., 2017, *MNRAS*, **472**, 876
- Ofman L., 2010, *Living Reviews in Solar Physics*, **7**, 4
- Oran R., Landi E., van der Holst B., Sokolov I. V., Gombosi T. I., 2017, *ApJ*, **845**, 98
- Parker E. N., 1958, *ApJ*, **128**, 664
- Pecaut M. J., Mamajek E. E., 2013, *ApJS*, **208**, 9
- Pizzolato N., Maggio A., Sciortino S., 2000, *A&A*, **361**, 614
- Pizzolato N., Maggio A., Micela G., Sciortino S., Ventura P., 2003, *A&A*, **397**, 147
- Powell K. G., Roe P. L., Linde T. J., Gombosi T. I., De Zeeuw D. L., 1999, *Journal of Computational Physics*, **154**, 284
- Pulkkinen T., 2007, *Living Reviews in Solar Physics*, **4**, 1
- Ramirez R. M., 2018, *Geosciences*, **8**, 280
- Ramstad R., Barabash S., 2021, *Space Sci. Rev.*, **217**, 36
- Redfield S., Linsky J. L., 2004a, *ApJ*, **602**, 776
- Redfield S., Linsky J. L., 2004b, *ApJ*, **613**, 1004
- Redfield S., Linsky J. L., 2008a, *The Astrophysical Journal*, **673**, 283
- Redfield S., Linsky J. L., 2008b, *ApJ*, **673**, 283
- Redfield S., Linsky J. L., 2015, *ApJ*, **812**, 125
- Reiners A., et al., 2022, *A&A*, **662**, A41
- Ribas I., Guinan E. F., Güdel M., Audard M., 2005, *ApJ*, **622**, 680
- Riley P., et al., 2014, *Sol. Phys.*, **289**, 769
- Sachdeva N., et al., 2019, *ApJ*, **887**, 83
- Schmidt K. H., Bögner M., Buschhorn G., Kotthaus R., Oberhuber R., Rzepka M., 1995, *Nuclear Instruments and Methods in Physics Research A*, **367**, 215
- See V., et al., 2019a, *ApJ*, **876**, 118
- See V., et al., 2019b, *ApJ*, **876**, 118
- See V., et al., 2019c, *The Astrophysical Journal*, **886**, 120
- Shields A. L., Ballard S., Johnson J. A., 2016, *Phys. Rep.*, **663**, 1
- Shulyak D., Reiners A., Wende S., Kochukhov O., Piskunov N., Seifahrt A., 2010, *A&A*, **523**, A37
- Skumanich A., 1972, *ApJ*, **171**, 565
- Sokolov I. V., et al., 2013, *ApJ*, **764**, 23
- Stelzer B., Damasso M., Scholz A., Matt S. P., 2016, *Monthly Notices of the Royal Astronomical Society*, **463**, 1844
- Stone E. C., Frandsen A. M., Mewaldt R. A., Christian E. R., Margolies D., Ormes J. F., Snow F., 1998, *Space Sci. Rev.*, **86**, 1
- Strugarek A., 2018, in Deeg H. J., Belmonte J. A., eds., *Handbook of Exoplanets*. p. 25, doi:10.1007/978-3-319-55333-7_25
- Strugarek A., 2021, *arXiv e-prints*, p. arXiv:2104.05968
- Suzuki T. K., 2006, *ApJ*, **640**, L75
- Tian F., 2008, in AAS/Division for Planetary Sciences Meeting Abstracts #40. p. 14.06
- Tóth G., van der Holst B., Huang Z., 2011, *ApJ*, **732**, 102
- Tóth G., et al., 2012, *Journal of Computational Physics*, **231**, 870
- Tóth G., et al., 2005, *Journal of Geophysical Research*, **110**, A12226
- Van Doorslaere T., et al., 2020, *Space Sci. Rev.*, **216**, 140
- Velli M., Pucci F., Rappazzo F., Tenerani A., 2015, *Philosophical Transactions of the Royal Society of London Series A*, **373**, 20140262
- Vidotto A. A., 2021, *Living Reviews in Solar Physics*, **18**, 3
- Vidotto A. A., Bourrier V., 2017, *MNRAS*, **470**, 4026
- Vidotto A. A., Jardine M., Morin J., Donati J. F., Lang P., Russell A. J. B., 2013, *A&A*, **557**, A67
- Vidotto A. A., Jardine M., Morin J., Donati J. F., Opher M., Gombosi T. I., 2014a, *MNRAS*, **438**, 1162
- Vidotto A. A., et al., 2014b, *Monthly Notices of the Royal Astronomical Society*, **441**, 2361
- Vidotto A. A., Fares R., Jardine M., Moutou C., Donati J. F., 2015, *MNRAS*, **449**, 4117
- Vidotto A. A., et al., 2016, *MNRAS*, **455**, L52
- Villadsen J., Hallinan G., Bourke S., Güdel M., Rupen M., 2014, *ApJ*, **788**, 112
- Villarreal D'Angelo C., Jardine M., See V., 2017, *Monthly Notices of the Royal Astronomical Society: Letters*, **475**, L25
- Wargelin B. J., Drake J. J., 2002, *ApJ*, **578**, 503
- Weber E. J., Davis Leverett J., 1967, *ApJ*, **148**, 217
- Wood B. E., 2004, *Living Reviews in Solar Physics*, **1**, 2
- Wood B. E., Müller H.-R., Zank G. P., Linsky J. L., 2002, *ApJ*, **574**, 412
- Wood B. E., Redfield S., Linsky J. L., Müller H.-R., Zank G. P., 2005a, *The Astrophysical Journal Supplement Series*, **159**, 118
- Wood B. E., Müller H. R., Zank G. P., Linsky J. L., Redfield S., 2005b, *ApJ*, **628**, L143
- Wood B. E., Müller H.-R., Redfield S., Edelman E., 2014, *ApJ*, **781**, L33
- Wood B. E., et al., 2021, *ApJ*, **915**, 37
- Wright N. J., Drake J. J., 2016, *Nature*, **535**, 526
- Wright N. J., Drake J. J., Mamajek E. E., Henry G. W., 2011a, *ApJ*, **743**, 48
- Wright N. J., Drake J. J., Mamajek E. E., Henry G. W., 2011b, *ApJ*, **743**, 48
- Wright N. J., Newton E. R., Williams P. K. G., Drake J. J., Yadav R. K., 2018a, *MNRAS*, **479**, 2351
- Wright N. J., Newton E. R., Williams P. K. G., Drake J. J., Yadav R. K., 2018b, *Monthly Notices of the Royal Astronomical Society*, **479**, 2351
- van Saders J. L., Ceillier T., Metcalfe T. S., Silva Aguirre V., Pinsonneault M. H., García R. A., Mathur S., Davies G. R., 2016, *Nature*, **529**, 181
- van Saders J. L., Pinsonneault M. H., Barbieri M., 2019, *ApJ*, **872**, 128
- van den Oord G. H. J., Doyle J. G., 1997, *A&A*, **319**, 578
- van der Holst B., Sokolov I. V., Meng X., Jin M., Manchester W. B. I., Tóth G., Gombosi T. I., 2014, *ApJ*, **782**, 81
- van der Holst B., Manchester W. B. I., Klein K. G., Kasper J. C., 2019, *ApJ*, **872**, L18

APPENDIX A: TRENDS WITH MAXIMUM RADIAL MAGNETIC FIELD

We have also quantified \overline{AS}_R and $\dot{M}_\star / R_\star^2$ as a function of the absolute maximum radial magnetic field strength ($|B_R|^{\max}$). It is important to also investigate $|B_R|^{\max}$, since the average radial magnetic field strength may suffer from cancellations, especially if the star has a symmetric surface magnetic field distribution. Figure A1 shows the simulated average Alfvén surface area (\overline{AS} , top) and the mass-loss rate per unit surface area ($\dot{M}_\star / R_\star^2$, bottom) as a function of the maximum absolute radial magnetic field on the stellar surface ($|B_R|^{\max}$). We see a trend where \overline{AS} and $\dot{M}_\star / R_\star^2$ increase with increasing magnetic field strength. We fit this trend to a power law by applying the bootstrap method used to derive this parameter as a function of the average radial magnetic field (similar to the procedure used in Sect. 3.1, Eqs. 3 and 4).

$$\log \overline{AS}_R = (0.44 \pm 0.05) \log |B_R|^{\max} + (0.54 \pm 0.08) \quad (\text{A1})$$

$$\log \dot{M}_\star / R_\star^2 = (0.83 \pm 0.07) \log |B_R|^{\max} - (0.48 \pm 0.10) \quad (\text{A2})$$

This paper has been typeset from a $\text{\TeX}/\text{\LaTeX}$ file prepared by the author.

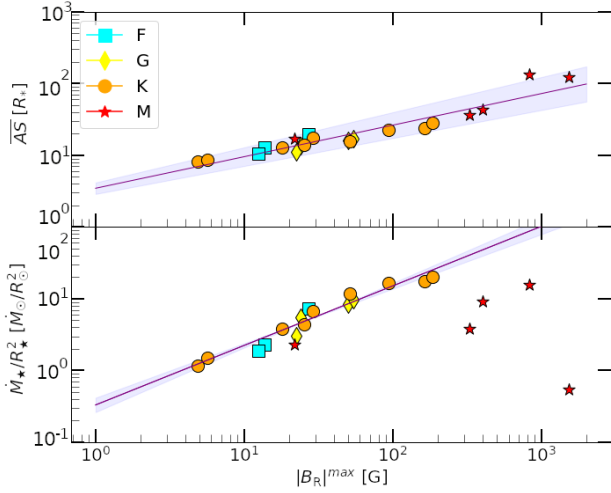


Figure A1. Simulated average Alfvén surface (\overline{AS} , top), and the mass loss rate per unit surface area ($\dot{M}_{\star}/R_{\star}^2$, bottom) as a function of the absolute surface-max radial magnetic field ($|B_R|^{\max}$). The mass loss rate is expressed in units of the average solar values, normalized to the surface area of each star. Individual points denote the results of each simulation presented in Sect. 3, Table 2. The different symbols and colors represent the spectral types (F, cyan/squares; G, yellow/diamonds; K, orange/circles; M, red/star). The purple line with the shaded purple area represents the fitted power-law with its uncertainties.